Photon emissivity in the vicinity of a critical point - A case study within the quark meson model

F. Wunderlich[a,b,*], B. Kämpfer[a,b]

[a] *Helmholtz-Zentrum Dresden-Rossendorf, Institute of Radiation Physics, Bautzner Landstr. 400, D-01328 Dresden, Germany*
[b] *Institut für Theoretische Physik, Technische Universität Dresden, D-01062 Dresden, Germany*

arXiv:1611.10139v1 [hep-ph] 30 Nov 2016

Abstract

The quark meson (linear sigma) model with linearized fluctuations displays at a critical end point the onset of a curve of first-order phase transitions (FOPTs) located at non-zero chemical potentials and temperatures below a certain cross-over temperature. The model qualifies well for an illustrative example to study the impact of the emerging FOPT, *e.g.* on photon emissivities. Such a case study unravels the tight interlocking of the phase structure with the emission rates, here calculated according to lowest-order tree level processes by kinetic theory expressions. It is the strong dependence of the rates on the effective masses of the involved degrees of freedom which distinctively vary over the phase diagram thus shaping the emissivity accordingly. At the same time, thermodynamic properties of the medium are linked decisively to these effective masses, *i.e.* a consistent evaluation of thermodynamics, governing for instance adiabatic expansion paths, and emission rates is maintained within such an approach.

Keywords: linear sigma model, quark meson model, chiral transition, real photon emission
PACS: 12.39.Fe, 13.60.-r, 13.60.Fz, 11.30.Qc

1. Introduction

After several decades of dedicated research, the phase diagram of QCD has revealed a number of fairly intricate properties. At zero baryo-chemical potential μ_B the Columbia plot (*cf.* [1, 2] for recent versions) points to a first ($m_s < m_s^{\rm tric}$) or second ($m_s \geq m_s^{\rm tric}$) order phase transition in the chiral limit for the light quark flavors, with the position of the tricritical point $m_s^{\rm tric}$ not yet settled, and to a crossover for physical quark masses when considering three quark flavors with the two light flavors being degenerate. In this way of thinking the case with all quark flavors set to infinity corresponds to pure gauge theory with a first-order phase transition (FOPT) at $T_c = \mathcal{O}(270\,\mathrm{MeV})$. Leaving the flavor number and quark mass dependence of T_c (either the cross over temperature scale or the critical temperature) to future investigations, much progress has been achieved for the relevant case with physical quark masses: $T_c = 154 \pm 8\,\mathrm{MeV}$ is now the settled continuum extrapolated cross over temperature [3, 4], where the description in terms of hadronic (quasi-particle) degrees of freedom has to be changed in favor of quark-gluon type degrees of freedom. Much less is known when allowing for non-zero baryo- (and maybe other) chemical potentials. Several techniques have been developed to access the region $\mu_B/T \lesssim 1$ [5–8]. A non-zero baryo-chemical potential μ_B is particularly intriguing as the cross over is expected to turn into a FOPT when moving to larger values of μ_B [9]. The onset can be related to a critical end point (CEP) with presently rather uncertain coordinates $(T_{\rm CEP}, \mu_{\rm CEP})$. Such an option of a CEP in the QCD phase diagram has triggered a lot of dedicated activities, both experimentally [10–13] and theoretically, applying lattice techniques *e.g.* reweighting [5], Taylor expansion in μ_B [8], analytic continuation from imaginary μ_B [6] or density of state methods [7] as well as Dyson-Schwinger [14], chiral model [15–20] or quasiparticle aproaches [21] giving widespread results [9]. One signature that is looked for is an unsteady behavior of event-by-event fluctuations of conserved quantities *e.g.* baryon number or strangeness [22, 23] and deviations from a Gaussian distribution of these parametrized by higher moments such as skewness and kurtosis [24]. An overview over possible approaches can be found in [25].

From the experimental side, there exist restrictions originating from astrophysical observations [26], nuclear physics and heavy-ion collisions (HICs). In the latter experiments, nuclei and protons in various combinations are brought to collision at relativistic energies and create a system of strongly interacting particles

*Corresponding author
Email addresses: f.wunderlich@hzdr.de (F. Wunderlich), kaempfer@hzdr.de (B. Kämpfer)

which expands rapidly and eventually fragments into hadrons. At RHIC and LHC energies, the hot medium produced initially is dense enough to be described in terms of nearly ideal relativistic hydrodynamics [27] leading to the notion that the quark-gluon medium is strongly coupled. By tuning the collision parameters (*e.g.* beam energy, centrality, system size etc.) the strongly interacting medium evolves through different parts of the phase diagram and thus peculiarities, such as phase boundaries and critical points, may leave imprints in the data. Transport [28] as well as hydrodynamical [29] calculations show indeed that the medium evolves through the region where chiral and confinement transitions presumably take place.

One tool for investigating the transiently hot and dense medium is provided by hadronic probes. Due to their strong interaction with the ambient medium they quickly loose the information of the conditions under which they where produced, but they can be used on the other hand to probe collective phenomena (*e.g.* elliptic and higher order flow components, jet quenching) and transport coefficients [30] as well as issues concerning strangeness production and quarkonia spectra. To obtain information from the hot and dense interior of the "fireball" created in HICs and proton-nucleus as well as high multiplicity proton-proton collisions, weakly interacting probes like photons or dileptons provide interesting tools (see [31–35] for recent reviews and further references). Due to their penetrating nature they monitor all stages in the course of such collisions rendering them very promising but rather difficult to analyze. While modern transport codes, *e.g.* UrQMD [36] or PHSD [37], try to calculate the photon (real and virtual) yields from several or even all states (pre-equilibrium photons, thermal photons from the hydrodynamical stage and photons from final state decays) [38, 39], other approaches focus on the thermalized stage applying kinetic theory [40, 41] or relate photon emission to the vector meson current via the assumption of vector meson dominance [42]. A detailed survey on the experimental status can be found in [43].

Recent analyses [44, 45] reveal a tension between the photon-v_2 measurements (pointing to late emission, when the medium anisotropy has built up) and the p_T systematics (pointing to earlier emission, when the medium is hotter). As a solution to this puzzle the authors in [44, 46] suggest a "critical enhancement" and the "semi-quark-gluon plasma"; another option is explored in [47].

For macroscopic systems an otherwise transparent medium becomes opaque near or at a critical point. This critical opalescence is a consequence of fluctuations on all length scales which is typically phrased as the correlation length becoming divergent at criticality [48, 49]. Guided by such a phenomenon, one can ask whether an equivalent effect may emerge also in a strongly interacting medium. In fact, in [50] such a possibility has been discussed in the context of pion condensation in compressed nuclear matter. Having in mind, however, HICs with rapid expansion dynamics, specific features of the photon emissivity, when passing nearby or through a critical point, are expected to be masked by pre- and post-critical contributions to the time integrated emission rate. We, therefore, focus here on the question whether the CEP-related FOPT causes peculiarities of the photon emission; in the best case such peculiarities could be strong enough that they show up even in integrated rates. Since our understanding of QCD in the region of interest is in its infancies, as mentioned above, we have to resort to a model which mimics at least a few of the desired effects, especially the onset of a FOPT. In the present study we select a special quark-meson model and account for linearized meson fluctuations. That is quarks and mesons contribute both to the pressure (contrary to the mean field approximation which, in the context of this model, discards the mesonic fluctuation contributions) thus allowing for a treatment within effective kinetic theory to calculate photon production by the respective quasi-particle modes.

Our paper is organized as follows. In Section 2 we define the employed quark-meson model including the electromagnetic sector. In Section 3 we derive an approximation of the generating functional for correlation functions, which is used in Section 4 to derive an expression for the leading order contributions of the photon production rate. The photon spectra are evaluated and discussed in Section 5. In the spirit of a crosscheck we give in Appendix B expressions for the grand canonical potential, which is tightly related to the generating functional and compare the thermodynamic potential with literature. Finally, we summarize in Section 7 after a brief discussion Section 6. Formal manipulations needed for the propagators as well as the derivative expansion of the fermion determinant are explained in Appendix A.1 and Appendix A.2. Some further details of the thermodynamics of the employed model are relegated to Appendix B. The squared matrix elements employed in the calculation of the photon rates are listed in Appendix C.

2. Model definition

To answer the question to which extent the photon signal can reflect the peculiarities of a phase diagram with a FOPT we resort to a specific model containing fermionic ("quark") and bosonic ("meson") degrees of

freedom. Its Lagrangian reads (τ_i are the Pauli matrices)

$$\mathscr{L} = \mathscr{L}_\psi + \mathscr{L}_{\rm km} - U(\sigma,\vec{\pi}), \tag{1}$$

$$\mathscr{L}_\psi = N_c\overline{\psi}(i\partial\!\!\!/ - g(\sigma + i\gamma^5\vec{\tau}\vec{\pi}))\psi \;\equiv\; N_c\overline{\psi}\big(G_\psi^0\big)^{-1}_{\sigma,\pi}\psi, \tag{2}$$

$$\mathscr{L}_{\rm km} = \frac{1}{2}\partial_\mu\sigma\partial^\mu\sigma + \frac{1}{2}\partial_\mu\vec{\pi}\partial^\mu\vec{\pi}, \tag{3}$$

$$U = \frac{\lambda}{4}(\sigma^2 + \vec{\pi}^2 - \zeta)^2 - H\sigma, \tag{4}$$

where we define the operator $\big(G_\psi^0\big)^{-1}_{\sigma,\pi} = (i\partial\!\!\!/ - g(\sigma + i\gamma^5\vec{\tau}\vec{\pi}))$ at given meson fields. The field ψ is a doublet of fermion fields with degeneracy N_c (which is interpreted in the context of strong interactions as the number of colors), while σ and $\vec{\pi}$ are iso-scalar and iso-vector spin-0 fields. The parameters g and λ characterize the strength of the fermion-meson coupling and the sigma-pion coupling, respectively, while the two other parameters are measures for the explicit (H) and spontaneous (ζ) breaking of chiral symmetry. In the literature, the model is often called the quark meson model (QMM) or the linear sigma model, although the latter notion sometimes only refers to the purely mesonic model with the Lagrangian $\mathscr{L}_{\rm km} - U$, which we call the $O(4)$ model.

With the field content just described, the low temperature properties do not agree well with observations at nuclear density or from neutron stars *e.g.* the pressure at low temperature is too small [51]. A systematic improvement can be achieved by including axial and vector mesons [52], enlarging the flavor space to three [53] or even four [54, 55] dimensions and including various symmetry breaking terms for fitting vacuum properties of the model to QCD results or meson properties [52]. The interaction with the gluon field can be partially included by coupling the QMM to a Polyakov loop for which several choices for the potential are possible [17, 18], *cf.* also [56]. Sometimes even glueballs are introduced [57]. The QMM as well as its various extensions are used as tools for mimicking (de-)confinement, chiral symmetry breaking and restoration [18] as well as their interplay, *e.g.* the closeness of the respective pseudocritical regions, properties of their critical points (such as critical exponents) [58], the influence of external control parameters such as magnetic fields [59–61], or its interplay with hydrodynamical models [62, 63].

For addressing the aforementioned question of phase structure imprints on the photon rate, the model has to be supplemented with an electromagnetic sector. Following [60, 61], we do so by replacing the partial derivative ∂^μ by the $U(1)$-covariant derivative $D^\mu = \partial^\mu - ieQA^\mu$ (e being the electromagnetic coupling strength and Q the charge operator) and by adding the conventional kinetic term for the gauge field (the photon field) A^μ with the field strength tensor $F^{\mu\nu} = \frac{i}{e}\Big[D^\mu, D^\nu\Big]$. This procedure corresponds to adding the terms $\mathscr{L}_{k\gamma}$ and $\mathscr{L}_e$ to the Lagrangian (1):

$$\mathscr{L}_{\rm eQMM} = \mathscr{L} + \mathscr{L}_{k\gamma} + \mathscr{L}_e, \tag{5}$$

$$\mathscr{L}_{k\gamma} = -\frac{1}{4}F^{\mu\nu}F_{\mu\nu}, \tag{6}$$

$$\mathscr{L}_e = N_c\overline{\psi}eQA\!\!\!/\psi + ieA^\mu\pi^-\partial_\mu\pi^+ - ieA_\mu\pi^+\partial^\mu\pi^- - e^2A_\mu A^\mu\pi^+\pi^-. \tag{7}$$

Having defined the model by $\mathscr{L}_{\rm eQMM}$ we go on by calculating the Euclidean generating functional S_η for correlation functions. We base our calculation on the path integral representation of S_η, but go beyond the standard mean field approximation (MFA) and include lowest order fluctuations of the meson fields. This seems necessary for the purpose of photon emission, since the electromagnetic field is expected to couple via derivatives to the charged pions, which are absent in the MFA approach.

3. The generating functional

As mentioned above we go beyond MFA following the approximation scheme introduced in [64]. For this purpose we have to calculate the photon emission in a consistent way. We achieve this goal by calculating the generating functional for Euclidean correlation functions to which we can adopt - due to the formal similarity of the generating functional and the partition function - the approximations for the partition function made in [64]. By functional differentiation we then derive the photon propagator consistent with this approximation and apply the McLerran-Toimela formula (see (47) below) to calculate the photon emission rate.

The path integral representation of the Euclidean generating functional for finite temperature and densities reads [65, 66]

$$\begin{aligned} S_\eta &\equiv S[\eta_\sigma, \vec{\eta}_\pi, \eta_q, \overline{\eta}_q, \eta_\gamma^\mu] \\ &= \int \mathscr{D}\overline{\psi}\mathscr{D}\psi\mathscr{D}\sigma\mathscr{D}\vec{\pi}\mathscr{D}[A] \\ &\quad \times \exp\left\{ -\int_0^\beta d\tau \int_{\mathbb{R}^3} d^3x \mathscr{L}_{\mathrm{eQMM}}(q,\overline{q},\sigma,\pi) + \mu\overline{\psi}\gamma^0\psi + \overline{q}\eta_q + \overline{\eta}_q q + \eta_\sigma\sigma + \eta_a^\pi\pi^a + \eta_\mu^\gamma A^\mu \right\}, \end{aligned} \tag{8}$$

where β is the inverse temperature T^{-1} and $\eta_\sigma, \vec{\eta}_\pi, \eta_q, \overline{\eta}_q, \eta_\gamma^\mu$ denote the sources of the respective fields. (The measure $\mathscr{D}[A]$ refers to an path integral over gauge independent field configurations, see [67].) The source term for the pions, $\vec{\eta}_\pi\vec{\pi} = \eta_\pi^1\pi_1 + \cdots + \eta_\pi^3\pi_3$, can be rewritten in terms of the charged pions according to $\vec{\eta}_\pi\vec{\pi} = \eta_\pi^-\pi^+ + \eta_\pi^+\pi^- + \eta_\pi^0\pi^0$ with $\chi^\pm = \sqrt{2}^{-1}(\chi^1 \mp i\chi^2)$, $\chi^0 = \chi^3$ and $\chi \in \{\pi, \eta_\pi\}$.

3.1. Integrating out the photons

The path integral over the photon field configurations being quadratic in the fields (for the gauge fixing, the standard covariant choice $\mathscr{L}_{\mathrm{fix}} = \xi^{-1}(\partial A)^2$ is made) can be evaluated exactly leading to

$$\begin{aligned} S_\eta = &\int \mathscr{D}\overline{\psi}\mathscr{D}\psi\mathscr{D}\sigma\mathscr{D}\vec{\pi}\sqrt{\det\left(G_\gamma^0\right)_{\mu\nu}} \\ &\times \exp\left\{ \int dx^4 \left(\mathscr{L} - \mu\overline{\psi}\gamma^0\psi + \overline{\eta}_q\psi + \overline{\psi}\eta_q + \eta_\sigma\sigma + \vec{\eta}_\pi\vec{\pi} \right) \right\} \\ &\times \exp\left\{ \int dz^4 dz'^4 (J_\gamma^\mu(z) + \eta_\gamma^\mu(z)) \left(G_\gamma^0\right)_{\mu\nu}(z,z') (J_\gamma^\nu(z') + \eta_\gamma^\nu(z')) \right\} \end{aligned} \tag{9}$$

with the electromagnetic current

$$J_\gamma^\mu(z) = -\overline{\psi}(z)e\hat{Q}\gamma^\mu\psi(z) - \pi^+(z)ie\partial^\mu\pi^-(z) + \pi^-(z)ie\partial^\mu\pi^+(z) \tag{10}$$

and the perturbative photon propagator $\left(G_\gamma^0\right)_{\mu\nu}$ formally defined by

$$\left(G_\gamma^0\right)_{\mu\nu}^{-1} = \left[g_{\mu\nu}\Box - \left(1 - \xi^{-1}\right)\partial_\mu\partial_\nu - e^2\pi^+\pi^- g_{\mu\nu} \right]. \tag{11}$$

3.2. Integrating out the fermions

The next step is to integrate out the quarks resulting in a fermion determinant, which is written as the exponential of a functional trace (*i.e.* a momentum-integral of traces over internal (*i.e.* Dirac- and flavor-) indices) and an exponential with source terms:

$$\begin{aligned} S_\eta = &\int \mathscr{D}\sigma\mathscr{D}\vec{\pi}\sqrt{\det\left(G_\gamma^0\right)_{\mu\nu}} \\ &\times \exp\left\{ \int dx^4 \left(\mathscr{L}_{\mathrm{km}} - U - \left(\mathrm{Tr}\ln\left(G_\psi^0\right)_{\sigma,\pi} \right)(x,x) + \eta_\sigma\sigma + \vec{\eta}_\pi\vec{\pi} \right) \right\} \\ &\times \exp\left\{ \int dz^4 dz'^4 (J_\gamma^\mu(z) + \eta_\gamma^\mu(z)) \left(G_\gamma^0\right)_{\mu\nu}(z,z') (J_\gamma^\nu(z') + \eta_\gamma^\nu(z')) + \overline{\eta}_q(z) \left(G_\psi^0\right)_{\sigma,\pi}(z,z') \eta_q(z') \right\}, \end{aligned} \tag{12}$$

with the quark propagator defined in (2). Up to now the evaluation is exact. But, since the remaining mesonic part is not at all a Gaussian integral, we are forced to employ several approximations in order to proceed.

3.3. Derivative expansion of the fermion trace

The term $\mathrm{Tr}\ln\left(G^0_\psi\right)_{\sigma,\pi}$ in (12) is expanded w.r.t. derivatives of the meson fields similar to [68, 69] yielding (see Appendix A.1 for details)

$$\mathrm{Tr}\ln\left(G^0_\psi\right)_{\sigma,\pi} = \mathrm{Tr}\ln\left[i\partial\!\!\!/ - m_q(\sigma,\vec{\pi})\right] + \mathscr{O}(\partial\sigma,\partial\vec{\pi}) \tag{13}$$

$$= \frac{1}{3(2\pi)^3}\int dp^3 \frac{p^2}{E_q}(1+n_F(E_q)+n_{\overline{F}}(E_q)) + \mathscr{O}(\partial\sigma,\partial\vec{\pi}), \tag{14}$$

$$E_q^2 = m_q^2 + p^2, \tag{15}$$

$$m_q^2 = g^2(\sigma^2+\vec{\pi}^2). \tag{16}$$

Assuming slowly varying meson fields the terms containing meson derivatives can be regarded small and are thus excluded from further calculations.

3.4. Quadratic approximation of the meson potential

The generating functional in (12) can be regarded as the generating functional of a purely mesonic theory with the potential V:

$$V(z) = U_{\mathrm{eff}}(\sigma(z),\pi(z)) - \int dz'^4 J^\mu_\gamma(z)\left(G^0_\gamma\right)_{\mu\nu}(z,z')J^\nu_\gamma(z'), \tag{17}$$

$$U_{\mathrm{eff}} = U(\sigma,\vec{\pi}) - \Omega_\psi(\sigma,\vec{\pi}), \tag{18}$$

$$\Omega_\psi = \frac{2N_F N_c}{3(2\pi)^3}\int dp^3 \frac{p^2}{E_q}\Big(1+n_F(E_q)+n_{\overline{F}}(E_q)\Big). \tag{19}$$

The effective potential U_{eff} is approximated by a quadratic potential $\overline{U}$ defined by the conditions

$$\langle\overline{U}\rangle = \langle U_{\mathrm{eff}}\rangle, \tag{20}$$

$$\left.\frac{\partial\overline{U}}{\partial\sigma,\pi}\right|_{\substack{\sigma=\langle\sigma\rangle\\ \vec{\pi}=0}} = 0, \qquad \text{with } \langle\sigma\rangle \text{ determined by} \qquad \left\langle\frac{\partial U_{\mathrm{eff}}(\langle\sigma\rangle+\Delta,\vec{\pi})}{\partial\Delta,\pi}\right\rangle = 0 \tag{21}$$

and with $\langle f(\sigma,\vec{\pi})\rangle$ being the ensemble average w.r.t. σ and $\vec{\pi}$ configurations according to the self consistently chosen probability density ρ given below in (26) (*cf.* (29) below for the averaging). The condition (20) fixes the zero-order coefficients in $\overline{U}$ and (21) the first order coefficients. The non-vanishing second order coefficients (which we name m_σ^2 and m_π^2) have to be chosen according to

$$\frac{\partial^2\overline{U}}{\partial\sigma^2} \equiv m_\sigma^2 = \left\langle\frac{\partial^2 U_{\mathrm{eff}}}{\partial\sigma^2}\right\rangle, \qquad \frac{\partial^2\overline{U}}{\partial\pi^2} \equiv m_\pi^2 = \left\langle\frac{\partial^2 U_{\mathrm{eff}}}{\partial\pi^2}\right\rangle \tag{22}$$

for being consistent to the respective propagator pole mass (see (36) below), calculated for the approximated theory with Lagrangian

$$\overline{\mathscr{L}} = \mathscr{L}_{\mathrm{km}} - \overline{U}(\sigma,\pi). \tag{23}$$

The 2nd order mixed term in U_{eff} vanishes, since U_{eff} is an even function of $\vec{\pi}$ as the inspection of (4), (16) and (18) reveals. The thus defined approximate potential

$$\overline{U} = \langle U_{\mathrm{eff}}\rangle + \frac{1}{2}m_\pi^2(\vec{\pi}^2 - \langle\vec{\pi}^2\rangle) + \frac{1}{2}m_\sigma^2(\sigma^2 - \langle\sigma^2\rangle) \tag{24}$$

induces via the accordingly approximated partition function $\overline{Z}$ a probability distribution ρ for the meson fields (for further convenience we chose to shift the sigma field by its thermal expectation value, $\sigma = \Delta + \langle\sigma\rangle$)

$$\rho(\sigma,\vec{\pi}) = \overline{Z}^{-1}\exp\left\{\int dx^4 \mathscr{L}_{km} - \overline{U}\right\} \tag{25}$$

$$= \frac{1}{\sqrt{2\pi\langle\Delta^2\rangle}}\exp\left\{\frac{-\Delta^2}{2\langle\Delta^2\rangle}\right\}\sqrt{\frac{2}{\pi}\left(\frac{3}{\langle\vec{\pi}^2\rangle}\right)^3}\exp\left\{\frac{-3\vec{\pi}^2}{2\langle\vec{\pi}^2\rangle}\right\}, \tag{26}$$

where we already exploited the fact that all relevant functions are even functions of $\vec{\pi}$, leading to the following form of the variances ($\mathrm{var}\, f = \langle f^2\rangle - \langle f\rangle^2$) for the meson fields

$$\langle \Delta^2\rangle = \mathrm{var}\,\sigma = \frac{1}{(2\pi)^3}\int d^3p \left(\frac{1}{2E_\sigma} + \frac{1}{E_\sigma} n_B(E_\sigma)\right), \tag{27}$$

$$\langle \vec{\pi}^2\rangle = 3\,\mathrm{var}\,\pi_i = \frac{3}{(2\pi)^3}\int d^3p \left(\frac{1}{2E_\pi} + \frac{1}{E_\pi} n_B(E_\pi)\right), \tag{28}$$

with the dispersion relations $E^2_{\sigma,\pi} = m^2_{\sigma,\pi} + \vec{p}^2$. With (26) the ensemble averages $\langle f\rangle$ of a meson dependent function can be calculated according to

$$\langle f(\sigma,\vec{\pi})\rangle = \int d\Delta \int d|\vec{\pi}|\rho(\Delta + \langle\sigma\rangle, |\vec{\pi}|) f(\Delta + \langle\sigma\rangle, |\vec{\pi}|), \tag{29}$$

where we let f only depend on $|\vec{\pi}|$, since that is the only case relevant for our calculation. Equations (27) and (28) represent consistency conditions for the choice of the second order coefficients, *i.e.* the meson mass parameters, as they can be calculated via the induced probability distribution (26) as well as by differentiation of the thermodynamical potential (which is related to the generating functional, as discussed below in Appendix B). The equations (21), (22), (27) and (28) represent a set of five equations for m_π, m_σ, $\langle\sigma\rangle$, $\langle\Delta^2\rangle$ and $\langle\vec{\pi}^2\rangle$ which have to be solved simultaneously (*cf.* [64], eqs. (51), (52), (17), (37) and (38) with (42) and (47) inserted into (17)). The quark source term in (12) is treated by expanding $\left(G^0_\psi\right)_{\sigma,\pi}$ w.r.t. the meson fields (*cf.* Appendix A.2) and replacing the meson fields afterwards by the variation w.r.t. the corresponding sources.

3.5. Isolating the electromagnetic contribution

We now want to treat the electromagnetic contribution in (17) as a small perturbation to S_η. Therefore, we first expand (*cf.* Appendix A.2) the photon propagator $\left(G^0_\gamma\right)_{\mu\nu}$ w.r.t. powers of e^2 and afterwards the exponential of the current term into a Taylor series:

$$\exp\left\{\int dz^4 dz'^4 (J^\mu_\gamma(z) + \eta^\mu_\gamma(z))\left(G^0_\gamma\right)_{\mu\nu}(z,z')(J^\nu_\gamma(z') + \eta^\nu_\gamma(z'))\right\} \tag{30}$$

$$= 1 + \int dz^4 dz'^4 (J^\mu_\gamma(z) + \eta^\mu_\gamma(z))\Big(\overline{G}^\gamma_{\mu\nu}(z,z') + e^2\int dz'' \overline{G}^\gamma_{\mu\rho}(z,z'') g^{\rho\kappa}\pi^+(z'')\pi^-(z'')\overline{G}^\gamma_{\kappa\nu}(z'',z') + \mathscr{O}\left(e^4\right)\Big)(J^\nu_\gamma(z') + \eta^\nu_\gamma(z')) + \mathscr{O}\left(J^4_\gamma\right). \tag{31}$$

Since $J^\mu_\gamma = \mathscr{O}(e)$ the terms up to $\mathscr{O}\left(e^2\right)$ are

$$\exp\left\{\int dz^4 dz'^4 (J^\mu_\gamma(z) + \eta^\mu_\gamma(z))\left(G^0_\gamma\right)_{\mu\nu}(z,z')(J^\nu_\gamma(z') + \eta^\nu_\gamma(z'))\right\} \tag{32}$$

$$= 1 + \int dz^4 dz'^4 (J^\mu_\gamma(z) + \eta^\mu_\gamma(z))\overline{G}^\gamma_{\mu\nu}(z,z')(J^\nu_\gamma(z') + \eta^\nu_\gamma(z')) + \mathscr{O}\left(J^4_\gamma\right) + \int dz^4 dz'^4 \int dz''^4 \eta^\mu_\gamma(z) e^2 \overline{G}^\gamma_{\mu\rho}(z,z'') g^{\rho\kappa}\pi^+(z'')\pi^-(z'')\eta^\nu_\gamma(z)\overline{G}^\gamma_{\kappa\nu}(z'',z') + \mathscr{O}\left(e^3\right). \tag{33}$$

Finally, $\pi^+(z)\pi^-(z)$ is replaced by $\delta/\delta\eta^-_\pi(z)\delta/\delta\eta^+_\pi(z)$ and J by $\widehat{J}_\gamma$ as defined by

$$\widehat{J}_\gamma{}^\mu(z) = -\frac{\delta}{\delta\eta_q(z)} e\hat{Q}\gamma^\mu \frac{\delta}{\delta\overline{\eta}_q(z)} - \frac{\delta}{\delta\eta^-_\pi(z)} ie\partial^\mu \frac{\delta}{\delta\eta^+_\pi(z)} + \frac{\delta}{\delta\eta^+_\pi(z)} ie\partial^\mu \frac{\delta}{\delta\eta^-_\pi(z)}. \tag{34}$$

With this replacements, (33) can be pulled out of the path integral.

3.6. Integrating out the meson fields

The remaining integrand of the path integrals in (12) is Gaussian yielding

$$\begin{aligned} S_\eta =& \sqrt{\det\left(G_\gamma^0\right)_{\mu\nu}}\sqrt{\det {G_\pi}^3}\sqrt{\det G_\sigma}\exp\left\{-\int d^4x\langle U_{\text{eff}}\rangle+\frac{1}{2}m_\pi^2\langle\vec{\pi}^2\rangle+\frac{1}{2}m_\sigma\langle\Delta^2\rangle\right\}\\ &\times\exp\left\{\int dz^4dz'^4\left(\widehat{J_\gamma}^\mu(z)+\eta_\gamma^\mu(z)\right)\left(\widehat{G_\gamma^0}\right)_{\mu\nu}(z,z')\left(\widehat{J_\gamma}^\nu(z')+\eta_\gamma^\nu(z')\right)\right\} \qquad (35)\\ &\times\exp\left\{\overline{\eta}_q(z)\widehat{G_\psi^0}(z,z')\eta_q(z')+\eta_\sigma(z)G_\sigma(z,z')\eta_\sigma(z')+\eta_\pi^+(z)G_\pi(z,z')\eta_\pi^-(z')+\eta_\pi^0(z)G_\pi(z,z')\eta_\pi^0(z')\right\}, \end{aligned}$$

with $\widehat{G_\psi^0}$ and $\left(\widehat{G_\gamma^0}\right)_{\mu\nu}$ obtained from $\left(G_\psi^0\right)_{\sigma,\pi}$ and $\left(G_\gamma^0\right)_{\mu\nu}$ by replacing $\sigma\to\delta/\delta\eta_\sigma$ and $\pi^a\to\delta/\delta\eta_{\pi^{-a}}$. The momentum space meson propagators can be found by an explicit evaluation of the Gaussian meson path integrals yielding

$$G_\pi^{a\bar{b}}(p)=\frac{\delta^{ab}}{p^2-m_\pi^2}, \qquad G_\sigma(p)=\frac{1}{p^2-m_\sigma^2} \qquad (36)$$

with $a,b\in\{0,+,-\}$ denoting the charge of the respective pions, $\overline{b}\equiv -b$ and the mass parameters according to (22).

4. The imaginary part of the photon propagator

Having derived the formal basics we turn now to the derivation of photon emission rates. The wanted key quantity is the imaginary part of the retarded photon propagator which allows to cast the rates into a kinetic theory formula.

4.1. The photon propagator

The full photon propagator (within the above approximations), $\mathscr{G}$, can be calculated by varying S_η w.r.t. the photon sources:

$$\mathscr{G}_{\mu\nu}^\gamma(x,y)=\frac{1}{S}\frac{\delta^2}{\delta\eta_\gamma^\mu(x)\delta\eta_\gamma^\nu(y)}S_\eta. \qquad (37)$$

Executing the variations yields

$$\begin{aligned} \mathscr{G}_{\mu\nu}^\gamma(x,y)=&\overline{G}_{\mu\nu}^\gamma(x,y)+e^2\frac{1}{S}\int dz\overline{G}_{\mu\alpha}^\gamma(x,z)\frac{\delta}{\delta\eta_\pi^-(z)}\frac{\delta}{\delta\eta_\pi^+(z)}g^{\alpha\beta}\overline{G}_{\beta\nu}^\gamma(z,y)S_\eta\Big|_{\eta=0}\\ &+\frac{1}{S}\int dz\int dz'\overline{G}_{\mu\alpha}^\gamma(x,z)\widehat{J_\gamma}^\alpha(z)\widehat{J_\gamma}^\beta(z')\overline{G}_{\beta\nu}^\gamma(z',y)S_\eta\Big|_{\eta=0}, \qquad (38)\\ \left(\overline{G}_{\mu\nu}^\gamma\right)^{-1}=&\left[g_{\mu\nu}\Box-\left(1-\xi^{-1}\right)\partial_\mu\partial_\nu\right]=\left(G_\gamma^0\right)_{\mu\nu}{}^{-1}+e^2\pi^+\pi^-g_{\mu\nu}. \qquad (39) \end{aligned}$$

First we execute the variations w.r.t. the fermionic sources. The result can be represented diagrammatically as exhibited in Fig. 1 (upper panel). Looking at the upper panel of Fig. 1 we want to stress that it represents an intermediate step of the calculation and the (conventional) prescription that only connected diagrams contribute cannot be applied yet. Comparing the upper panel of Fig. 1 with (38) one can identify the first two diagrams with the first two terms in (38). The rest of the diagrams corresponds to the $\mathscr{O}\left(e^2\right)$ contributions of the second line of (38) with the derivatives w.r.t. the fermionic sources carried out. Since the fermionic sources appear only as $\exp\left\{\int\int dz^4dz'^4\overline{\eta}_q(z)\widehat{G_\psi^0}(z,z')\eta_q(z')\right\}$ in S_η, every pair of (functional) derivatives w.r.t. fermionic sources corresponds to a quark propagator $\widehat{G_\psi^0}$ connecting the space-time arguments of the source derivatives, exactly as it is conventionally done, *e.g.* in Feynman diagram calculus of QED correlation functions or self energy contributions. (However, since $\widehat{G_\psi^0}$ explicitly depends on meson source derivatives, disconnected fermionic loops can be connected in the next step by meson propagators leading to the lower panel of Fig. 1.) The fermion propagators represented by double lines are expanded according to (A.23). This

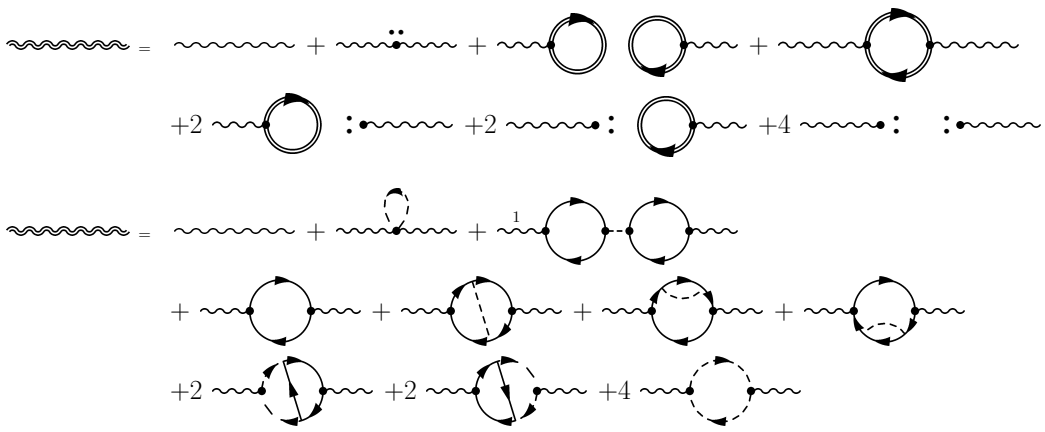

Figure 1: Upper panel: Diagrammatic representation of the electromagnetic current term in (38) after applying the fermion source derivatives and setting the fermion sources zero. Lower panel: Diagrammatic representation of the electromagnetic current term after additionally executing all meson source derivatives, both written down explicitly as dots next to a vertex and implicitly contained in the summed fermion propagator. Solid double lines represent the summed fermion propagator $\widehat{G^0_\psi}$, the double wavy line stands for the full photon propagator up to $\mathscr{O}\left(e^2\right)$ and $\mathscr{O}\left(g^2\right)$, the single solid lines represents $\left(G^0_\psi\right)_{\langle\sigma\rangle,0}$, single wavy lines the perturbative photon propagator $\overline{G}^\gamma_{\mu\nu}$, dashed lines represent a sum over all meson field propagators G_π and G_σ connected to the fitting vertices (dots). Arrows on dashed lines denote the direction of charge flow. (They appear only at lines connected to a photon vertex, so that only charged pions contribute to the diagram, for which the direction of charge flow is well defined.)

expansion follows from the decomposition of $\left(G^0_\psi\right)_{\sigma,\pi}$ into a part independent of the dynamical fields Δ and π (but dependent on the average σ field) and an interaction part that depends on Δ and π according to

$$\left(\left(G^0_\psi\right)_{\sigma,\pi}\right)^{-1} = \left(\left(G^0_\psi\right)_{\langle\sigma\rangle,0}\right)^{-1} - g(\Delta + i\gamma^5\vec{\tau}\vec{\pi}), \tag{40}$$

$$\left(\left(G^0_\psi\right)_{\langle\sigma\rangle,0}\right)^{-1} = i\partial\!\!\!/ - g\langle\sigma\rangle. \tag{41}$$

After doing all meson variations, symbolically denoted by dots next to the vertices in the upper panel of Fig. 1, every pair of derivatives w.r.t. meson sources reduces to a propagator of the respective meson (provided both variations are w.r.t. the same fields source). The resulting expression can be represented diagrammatically according to the lower panel of Fig. 1. There, each solid line represents $\left(G^0_\psi\right)_{\langle\sigma\rangle,0}$, each dashed line stands for $G_\sigma + G_\pi$, each wiggly line refers to $\overline{G}^\gamma_{\mu\nu}$ and each dot means the corresponding vertex factor.

4.2. Determining the imaginary part of the photon propagator

The propagators G_σ, G_π (see (36)) and $\left(G^0_\psi\right)_{\langle\sigma\rangle,0}$ (see (41)) have the form discussed in [70]. For the imaginary part of the diagrams in Fig. 1, one therefore has to cut through each diagram in any possible way that separates the two vertices connected to external photon lines. Such a procedure leads to sets of (simpler) diagrams corresponding to processes of the type $\phi_1,\ldots,\phi_a \to \Phi_1,\ldots,\Phi_b+\gamma$ with a incoming and $b+1$ outgoing field quanta, one of which is a photon. Denoting the diagrams in Fig. 1 by $\mathscr{M}^{(j)}_{\gamma\to\gamma}$ and the diagrams obtained from cutting these by $\mathscr{M}^{(j,l)}_{\phi_1+\cdots+\phi_a\to\Phi_1+\cdots+\Phi_b+\gamma}$ one arrives for $\mathrm{Im}\,\mathscr{G}^{\mu\nu}_{\gamma,\mathrm{ret}} \sim \sum_j \mathrm{Im}\,\mathscr{M}^{(j)}_{\gamma\to\gamma}$ at

$$\mathrm{Im}\,\mathscr{G}^{\mu\nu}_{\gamma,\mathrm{ret}} = 2\sum_{a,b,j,l}\int d\Omega_{ab}\,|\mathscr{M}^{(j,l)}_{\phi_1+\cdots+\phi_a\to\Phi_1+\cdots+\Phi_b+\gamma}|^2 n^{(i,1)}\cdots n^{(i,a)}(1\pm n^{(o,1)})\cdots(1\pm n^{(o,b)})(e^{\omega/T}-1), \tag{42}$$

$$\int d\Omega_{ab} = \int \frac{d^3p_1}{2E^{(1)}_p(2\pi)^3}\cdots\frac{d^3p_a}{2E^{(a)}_p(2\pi)^3}\,\frac{d^3q_1}{2E^{(1)}_q(2\pi)^3}\cdots\frac{d^3q_b}{2E^{(b)}_q(2\pi)^3}(2\pi)^4\delta\left(k-\sum_c p^c+\sum_d q^d\right), \tag{43}$$

with $n^{(i/o,l)}$ being Fermi or Bose distribution functions (depending on the spin of the particle l in the in (i) or out (o) state). The summands in (42) can be sorted w.r.t. the number $= a+b+1$ of participating fields. The inspection of the phase space regions over which one has to integrate on the rhs. of (42) yields zero for all summands with $a+b\leq 2$ since the phase space vanishes in these cases, at least if all field quanta - except the

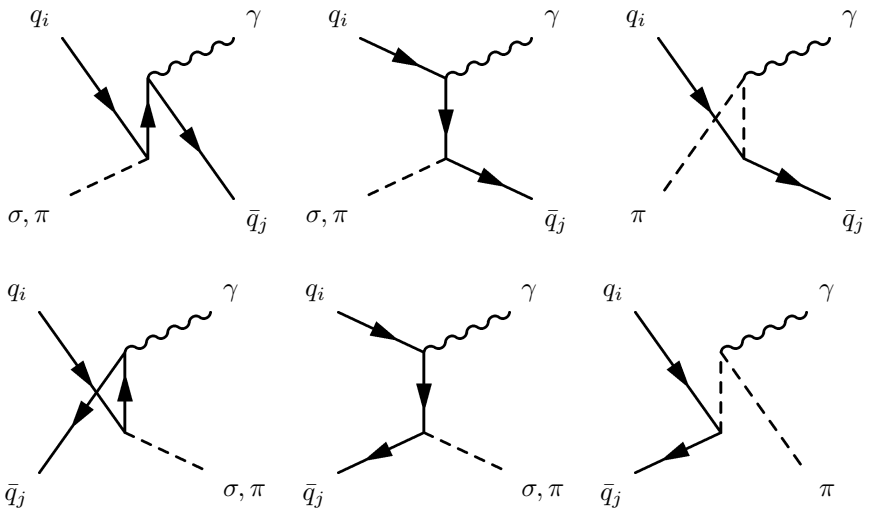

Figure 2: Tree-level diagrams of the reactions (44)-(46). Top row: diagrams for Compton scattering off quarks; bottom row: annihilations. The matrix elements for Compton scattering off antiquarks can be obtained by inverting the direction of the fermion arrows. Note that in the third column there is no σ meson, since it is uncharged.

photons - are massive (as it is the case in our model). The first non zero terms have $a+b=3$ and correspond to the $2\to 2$ processes

$$q_i+\sigma,\pi \to q_j+\gamma \qquad \text{(Compton scatterings off quarks)}, \tag{44}$$

$$\overline{q}_i+\sigma,\pi \to \overline{q}_j+\gamma \qquad \text{(Compton scatterings off antiquarks)}, \tag{45}$$

$$q_i+\overline{q}_j \to \sigma,\pi+\gamma \qquad \text{(annihilations)}. \tag{46}$$

The corresponding diagrams are depicted in Fig. 2, and the polarization, spin and flavor summed/averaged squared matrix elements are listed in Appendix C.

4.3. Photon emission rate

From the imaginary part of the photon propagator, the photon rate can be determined according to the McLerran-Toimela formula [71]

$$\omega\frac{d^7N}{d^3k d^4x}=\frac{g_{\mu\nu}}{(2\pi)^3}\mathrm{Im}\,G^{\mu\nu}_{\gamma,\mathrm{ret}}(k^2=0,\omega)n_B(\omega). \tag{47}$$

With (42) we get as the leading terms in the above mentioned expansion w.r.t. the number of participating particles

$$\omega\frac{d^7N}{d^3k d^4x}=2\frac{g_{\mu\nu}}{(2\pi)^{12}}\sum_{i,j}\int\frac{d^3p_1}{2E_p^{(1)}}\frac{d^3p_2}{2E_p^{(2)}}\frac{d^3q}{2E_q}(2\pi)^4\delta(k-p^1-p^2+q)|\mathscr{M}^{(i,j)}_{\phi_1+\phi_2\to\Phi_3+\gamma}|^2 n^{(1)}n^{(2)}(1\pm n^{(3)}) \tag{48}$$

which resembles the formula for the production of photons in $2\to 2$ processes within a kinetic theory approach.

One might ask the question of what we have achieved with the above derivation that goes beyond the mere use of formula (48) which could naively be used right from the beginning. The very necessity to derive (48) is to identify precisely the mass parameters m_σ, m_π, m_q to be used for the calculation of the photon rates. The meson masses have to be chosen to be the second order coefficients of the approximative potential $\overline{U}$ according to (22). However, the correct fermion mass is less obvious. Reference [64] suggests to use $M_n=(\langle m_q(\sigma,\vec{\pi})^n\rangle)^{1/n}$ for conveniently chosen values n without convincing justification for this choice. As the resulting quark mass does not strongly depend on n, we used $n=2$ in a previous work [72] on the subject. With the derivation above this issue can be settled by choosing

$$m_q=g\langle\sigma\rangle \tag{49}$$

[MeV]	$m_{\rm nuc}^{\rm vac}$	$m_\sigma^{\rm vac}$	$m_\pi^{\rm vac}$	$\langle\sigma\rangle_{\rm vac}$	$T_c(\mu=0)$	$\mu_c(T=0)$	$T_{\rm CEP}$	$\mu_{\rm CEP}$
A	936.0	700.0	138.0	92.4	148.3	328	72.5	279.5
B	1170.0	1284.4	138.0	90.0	194.6	430	97.0	377.5
C	1080.0	700.0	138.0	90.0	140.3	324	98.0	216.0

Table 1: Parameter sets used for the analysis. The parameters $m_{\rm nuc}^{\rm vac}$, $m_\sigma^{\rm vac}$, $m_\pi^{\rm vac}$, $\langle\sigma\rangle_{\rm vac}$ can be mapped to the parameters g, λ, ζ, H of the Lagrangian (1) by (51). These parameters yield the cross over temperature $T_c(\mu=0)$ at vanishing chemical potential, the critical chemical potential at zero temperature $\mu_c(T=0)$ and the coordinates for the CEP $(T_{\rm CEP},\mu_{\rm CEP})$ given in the last columns. All quantities are in units of MeV as indicated in the upper left corner of the table.

in order to arrive at a representation of the photon propagator in terms of Feynman diagrams which can simply be cut to obtain the imaginary part of each diagram leading to the kinetic-theory-like formula (48). In other words, one may say that the M_n can be regarded as "thermodynamical mass" parameters since they are reasonable choices to be used in thermodynamic integrals, but fail to be used in perturbative calculations as mass parameters for the quark propagators. Although the choice of n does affect M_n only sightly, there is a large difference between M_n and m_q in the chirally restored phase. (In the chirally broken phase the meson field fluctuations are smaller which brings M_n and m_q closer together.). Thus the validity of (48) relies on the consistent choice (49) for the mass parameter to be used in the fermion propagators.

5. Evaluation of photon rates

5.1. Parameter fixing

To be explicit one has to fix the parameters of the Lagrangian defined by (1)-(4). The simplest way to do so is to set the vacuum masses of the fields as well as the vacuum expectation value of the σ field to specific values. In mean field approximation and the linearized fluctuation approximation without vacuum fluctuations the relations between the parameters and the vacuum field properties can be given by the set of equations

$$(m_\sigma^{\rm vac})^2-(m_\pi^{\rm vac})^2=2\lambda\langle\sigma\rangle_{\rm vac}{}^2, \qquad (m_\sigma^{\rm vac})^2-3(m_\pi^{\rm vac})^2=2\lambda\zeta, \tag{50}$$

$$(m_\pi^{\rm vac})^2\langle\sigma\rangle_{\rm vac}=H, \qquad m_{\rm nuc}^{\rm vac}=3g\langle\sigma\rangle_{\rm vac}, \tag{51}$$

with the nucleon mass at $T=\mu=0$ taken as $m_{\rm nuc}^{\rm vac}=3m_q^{\rm vac}$. Typically, one chooses for $m_\sigma^{\rm vac}$, $m_\pi^{\rm vac}$ and $m_{\rm nuc}^{\rm vac}$ the PDG values [73] and $\langle\sigma\rangle_{\rm vac}=f_\pi$. However, this is not strictly required for making contact to QCD, since at low temperatures many other degrees of freedom are relevant, which could easily shift these values one way or the other thus giving some flexibility to the parameters as long as typical mass scales are kept at the order of Λ_{QCD}. Throughout this paper we use the values of $m_\sigma^{\rm vac}, m_\pi^{\rm vac}, m_{\rm nuc}^{\rm vac}$ and $\langle\sigma\rangle_{\rm vac}$ to identify the parameter sets, which are collected in Tab. 1.

5.2. Differential Spectra

In Fig. 3, the differential photon spectra $\omega d^7N/d^3kd^4x$ are depicted for the individual channels (44)-(46) as well as for their sum. A first inspection shows several aspects: (i) For large photon energies, $\omega\gtrsim 600\,$MeV, all partial rates decrease exponentially $\propto\exp\{-\omega/T\}$. (ii) In the chirally restored phase (see right panel of Fig. 3), the partial rates for processes involving different mesons are either approximately degenerate (for the annihilations) or differ only by a factor of about three. This is a manifestation of the chiral symmetry restoration which leads to approximately degenerate meson masses, which in turn lead to similar kinematics for the processes involving chiral partners. The difference between pion-involving and sigma-involving partial rates can be atributed to the different multiplicities and the charge carried by two of the pions. Conversely, in the chirally broken phase no such striking similarity can be observed (see left panel of Fig. 3). (iii) In the chirally restored phase, at $\omega\gtrsim 200\,$MeV there is a clear hierarchy of the rates from different processes: The partial rate from Compton processes with quarks is much larger than the partial rate from annihilations which is also much larger than the rate from Compton processes with anti-quarks. As pointed out in [72] the reason for this hierarchy is the exponential suppression of incoming anti-particles at finite chemical potential, leading to a suppression $\propto\exp\{-\mu/T\}$ of the annihilation processes and a suppression $\propto\exp\{-2\mu/T\}$ for the anti-Compton processes w.r.t. the partial rates from Compton processes with quarks. (iv) In the chirally restored phase the annihilation rates diverge at $\omega\to 0$, see right panel of Fig. 3. This is caused by infrared divergencies of the matrix elements which are exponentially suppressed $\propto\exp\{-1/\omega\}$ if the sum of the incoming masses is larger than the mass of the outgoing particle that is not a photon. Such an inequality holds necessarily for all Compton and anti-Compton processes but may be violated for the annihilation processes; *cf.* [72] for a further

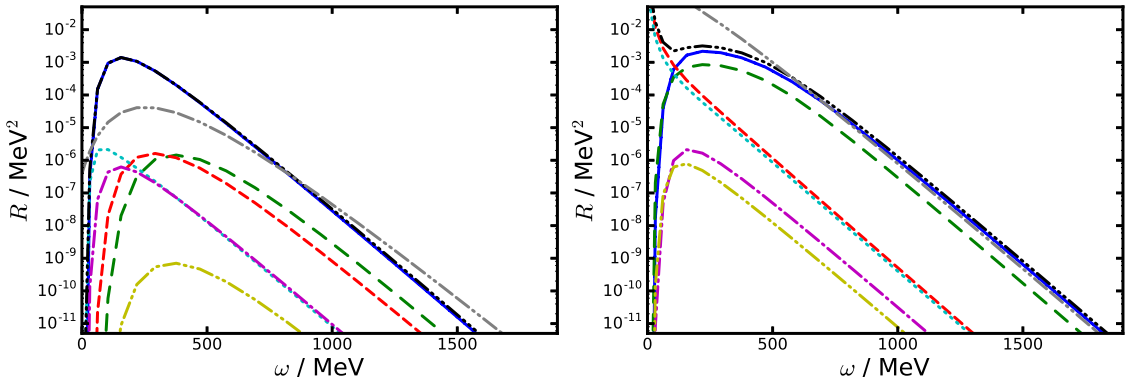

Figure 3: Differential photon spectra $R = \omega d^7N/d^3kd^4x$ as functions of photon energy ω for parameter set A. Left panel: chirally broken phase at $T = 65\,\mathrm{MeV}$ and $\mu = 255\,\mathrm{MeV}$; right panel: restored phase at $T = 65\,\mathrm{MeV}$ and $\mu = 295\,\mathrm{MeV}$. The curves correspond to the partial rates for the processes $\overline{q}+\sigma \to \overline{q}+\gamma$ (dash-double-dotted yellow curve), $\overline{q}+\pi \to \overline{q}+\gamma$ (dash-dotted violet curve), $q+\overline{q} \to \sigma+\gamma$ (dotted light blue curve), $q+\overline{q} \to \pi+\gamma$ (short dashed red curve), $q+\sigma \to q+\gamma$ (long dashed green curve), $q+\pi \to q+\gamma$ (solid dark blue curve) and to their sum (dash-triple dotted black curve), respectively. The gray double-dash-double-dotted curve in the left panel is calculated with the parametrization given in [74] and in the right panel it is the AMY rate [75] for which the strong coupling g_s was set to the value of the quark-meson coupling g of parameter set A. Since the masses $m_{\sigma,\pi,q}$ play an essential role for the photon emissivity we quote their values and supply the number densities in the heat bath rest frame:

	m_σ/MeV	m_π/MeV	m_q/MeV	$n_\sigma/\mathrm{fm}^{-3}$	n_π/fm^{-3}	n_q/fm^{-3}
left panel	504	151	282	2.65×10^{-5}	4.73×10^{-3}	0.205
right panel	283	333	55	3.93×10^{-4}	6.61×10^{-4}	0.971

discussion of that issue. For a comparison with rate calculations in the literature we exhibit in the left panel of Fig. 3 the rate calculated with the parametrization given in [74] for the emission from the hadronic phase and in the right panel the AMY rate [75] for the deconfined phase, however, for keeping the comparison as simple as possible both at $\mu = 0$.(For the strong coupling g_s in the AMY rate we use the value of the quark-meson coupling g, corresponding to $\alpha_s = 0.91$ for parameter set A.)

5.3. Photon rate over the phase diagram

Our central question is to which extent the features of the phase diagram are reflected in the photon emission rates. Therefore, we inspect the partial rates and their dependence on T and μ, *cf.* Figs. 4-6. As mentioned in Section 5.2 one sees a clear hierarchy of the emission rates for the different types of processes in the chirally restored phase. In the chirally broken phase the partial rate for the annihilation into π and γ is of similar size compared to the Compton processes, although it is suppressed by a factor of $\exp\{-\mu/T\}$. The reason for that is the comparatively small mass of the pions as the pseudo-Goldstone modes, which compensates for this suppression. The jump of the rates at the FOPT increases with decreasing temperature and reaches a factor of about 50 at the lowest displayed temperatures in the plots (see Fig. 4, right panels) for the dominating processes, *i.e.* the Compton processes, as well as for the total rate (see Fig. 7, right panel).

Only the annihilation process with σ mesons shows a non-monotonic behavior when scanning the partial rate along curves with constant T and varying μ. This can be traced back to the effective σ mass, which is relatively small in a valley surrounding the phase contour (FOPT and crossover region) and minimal at the CEP. Since the process $q+\overline{q} \to \sigma+\gamma$ is the only one of the considered channels that is primarily be influenced by the σ mass it is especially interesting for the search for CEP related features in the photon rates. However, the corresponding partial rate is strongly reduced by the above mentioned suppression factor $\exp\{-\mu/T\}$ relative to the Compton channels which makes is practically invisible in the total rate. This masking of the annihilation channels is expected to weaken drastically for parameter sets showing a CEP closer to the T axis.

6. Discussion

We have described an approximation scheme for calculating the thermodynamics and the effective masses of the fields contained in the QMM Lagrangian beyond the standard mean field approximation. The presented approximation scheme has been shown to be a consistent approximation for the determination of equilibrium thermodynamical properties and scattering or production rates. This makes the calculated meson masses applicable for S matrix calculations of the production rate for photons for which we present the lowest order

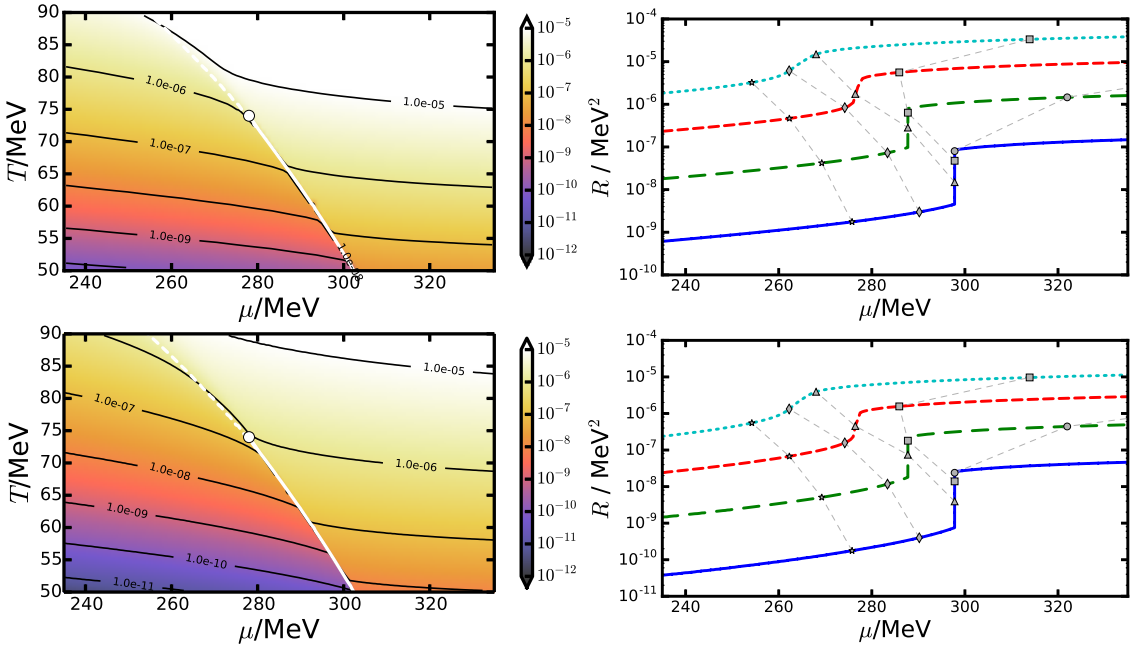

Figure 4: Photon emission rates $R = \omega d^7N/d^3kd^4x$ at $\omega = 1\,\mathrm{GeV}$ in the CEP region for the Compton processes $q+\pi \to q+\gamma$ (upper row), $q+\sigma \to q+\gamma$ (lower row). Left panels: contour plots of the rates in MeV^2; right panels: rates at constant temperature T/MeV =55, 65, 75 and 85 (bottom to top). The symbols denote the rates at isentropes with $s/n = 1.7$ (dots), 2.1 (squares), 2.5 (triangles), 2.9 (diamonds), 3.3 (stars) and the thin gray dashed curves are for guiding the eyes. Below, in Fig. B.8, these isentropes are displayed as black curves in the T-μ diagram. The solid white curves in the left plots depict the FOPT curves, and the white dashed line is an estimate of the crossover region based on the heat capacity. The dot depicts the position of the CEP, numerically determined by the coordinates of the minimum of the σ mass.

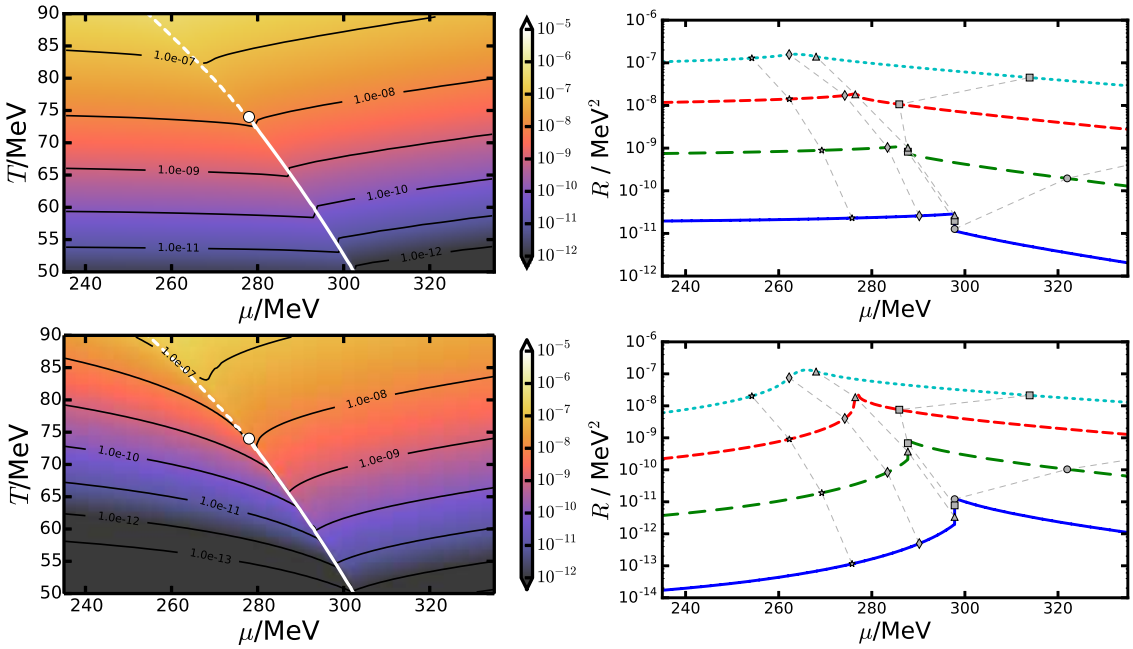

Figure 5: As Fig. 4, but for the annihilation processes $q+\overline{q} \to \pi+\gamma$ (upper row) and $q+\overline{q} \to \sigma+\gamma$ (lower row).

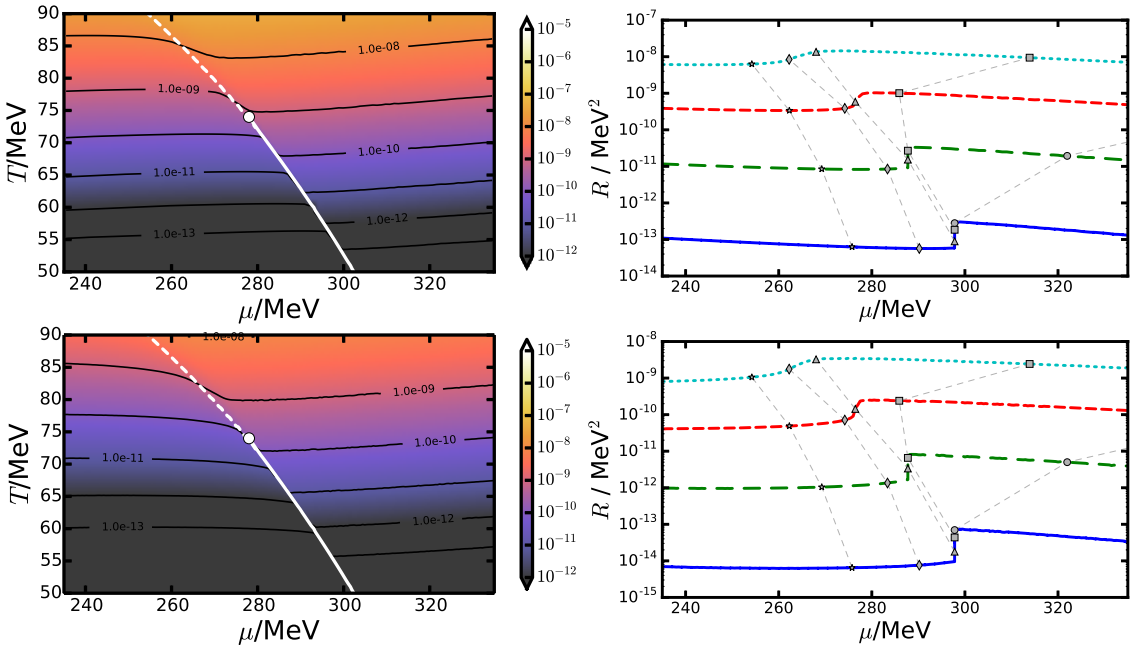

Figure 6: As Fig. 4, but for the anti-Compton processes $\overline{q}+\pi \to \overline{q}+\gamma$ (upper row) and $\overline{q}+\sigma \to \overline{q}+\gamma$ (lower row).

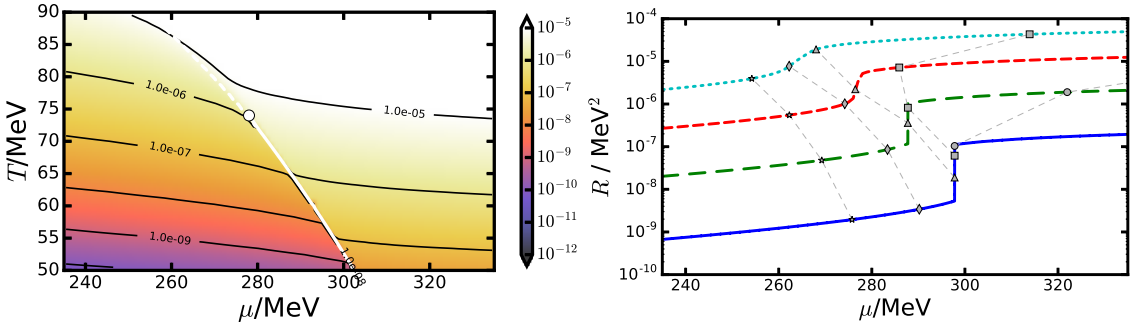

Figure 7: As Fig. 4, but for the sum of the processes of (44)-(46).

(in the electromagnetic as well as the quark-meson coupling) results. Furthermore, we discuss in Appendix B the influence of the model parameters on expansion properties provided by isentropes as well as on landmarks (such as position of the CEP, pseudocritical temperature at vanishing net density, general shape of the transition (first order as well as crossover) curve) of the phase diagram finding that all of these can be understood and adjusted to desired values with the help of two particular combinations of the parameters: the fermion vacuum mass $m_{\mathrm{nuc}}^{\mathrm{vac}}/3$ and the product of m_σ^{vac} and the vacuum expectation value of the sigma field $\langle\sigma\rangle_{\mathrm{vac}}$ as well as their interplay, at least for explicit symmetry breaking terms that are neither too small (*i.e.* $m_\pi^{\mathrm{vac}} \gtrsim 50\,\mathrm{MeV}$) to avoid being influenced by the wrong chiral limit, nor too big (*i.e.* $(m_\pi^{\mathrm{vac}}/m_\sigma^{\mathrm{vac}})^2 \ll 1$) in order for the QMM to invoke an only weakly broken chiral symmetry.

It turns out that in the intermediate photon energy range of $\omega \sim 1\,\mathrm{GeV}$ there are still sizable effects in the photon production rates due to a FOPT. Of course, for a firm result, many more emission channels have to be included (*e.g.* in [40], the channel $\pi^+\pi^- \to \sigma/\rho \to \pi^+\pi^-\gamma$ is identified to be important in the soft photon regime and in [76] $2 \to 3$ processes, such as meson-meson and meson-baryon bremsstrahlung, are found to be of great importance) and the effect of inclusion of higher order terms in the quark-meson coupling has to be checked as well as the effect of including further fluctuations (as done, *e.g.* in [77] within the FRG framework). In a previous work [72] we showed that the dominant effect on the photon rates stems from the mass variations and the explicit μ dependencies of the distribution function; in other words it is of kinematical origin. This leads us to the conjecture that the position and size of the discontinuities in the photon rate is a robust feature and could probably provide a tool suitable for the detection of a chiral FOPT in HIC experiments.

7. Summary

In summary, we employ here a quark-meson model with linearized fluctuations of the meson fields, which displays the onset of a curve of FOPTs at a (albeit imperfect) CEP. The thermodynamics has been elaborated in previous works [64, 72, 78–80]. We couple the pertinent degrees of freedom to the electromagnetic field to evaluate the photon emission rates over the phase diagram, in particular the impact of the FOPT. The chain of approximations is pointed out to arrive at emission rates in the form of kinetic theory expressions being consistent with the thermodynamics. To this end it is necessary to go beyond the mean field approximation, because in such an approach the mesons are no dynamic fields which is conceptually inconsistent with their usage in S matrix calculations. The first step in a path integral approach beyond mean fields is the inclusion of the lowest order fluctuations, which we achieve by the quadratic approximation of the effective mesonic potential. Our calculation differ from that in [64, 78, 79] by the inclusion of photons and the source terms for all fields (see Appendix B). The source terms make it possible to derive thermodynamics and S matrix elements on the same footing thus achieving consistency between both. Especially we can pin down the correct quark mass parameter for the calculation in the kinetic theory framework, which was not possible in previous works.

Due to the tight coupling of emissivities in lowest-order tree-level diagrams and thermodynamics, it happens that individual channels of photon producing processes map out the phase diagram. The emission rates are determined essentially by the effective masses of the involved field modes. While soft photons are either suppressed by finite temperature effects or enhanced by infrared divergencies of the matrix elements, the hard photons display the usually expected exponential shapes. Chiral restoration as degeneracy of pion and sigma effective masses causes also a degeneracy of the partial rates in the restored phase. The hard photon rates obey in the chirally restored phase for $\mu/T \gtrsim 1$ the following hierarchy: The rates from Compton-processes are larger than those from annihilations, which in turn are larger than those from anti-Compton processes.

We supplement our study by a discussion of the parameter dependence of the CEP coordinates and the location of the FOPT curve as well as the pattern of isentropic curves relevant for adiabatic expansion paths in the phase diagram (see Appendix B).

Finally, we mention that our investigation should be considered as a case study, not mimicking QCD features sufficiently adequate. Beyond the impact of vacuum fluctuations, the involved degrees of freedom mistreat (i) at low temperatures the nucleons and their incompressibility, as well as the other known hadronic states needed to saturate the equation of state known from QCD, and (ii) at high temperatures the explicit gluon degrees of freedom. Nevertheless, we stress again that a seemingly universal emissivity must not be combined with an ad hoc assumed thermodynamics/phase structure, however both issues must be dealt with in a consistent manner.

Acknowledgments

We thank J. Randrup, V. Koch, F. Karsch, K. Redlich, M.I. Gorenstein, S. Schramm, H. Stöcker, B.J. Schaefer, B. Friman, R. Rapp, H. van Hees and C. Gale for enlightening discussions of phase transitions in nuclear matter and photon emission. The work is supported by BMBF grant 05P12CRGH and TU Dresden graduate academy scholarship grant F-003661-553-62A-2330000.

Appendix A. A few formal details

Appendix A.1. Derivative expansion

In the case of a ϕ^4 theory the method is explained in [68, 69]. For convenience we outline it here and apply it to the theory at hand. The quantity we want to approximate is

$$\Omega_\psi = -\mathrm{Tr}\ln\left[\left(G^0_\psi(\sigma,\vec{\pi})\right)^{-1}\right] \tag{A.1}$$

with $\left(G^0_\psi(\sigma,\vec{\pi})\right)^{-1}$ defined according to (2). Formally we can expand

$$\begin{aligned}
\Omega_q &= -\mathrm{Tr}\ln\left[i\partial\!\!\!/ - g(\sigma + i\gamma^5\vec{\tau}\vec{\pi})\right] && \text{(A.2)}\\
&= -\mathrm{Tr}\ln\left[i\partial\!\!\!/\left(1 - \frac{1}{i\partial\!\!\!/}g(\sigma + i\gamma^5\vec{\tau}\vec{\pi})\right)\right] && \text{(A.3)}\\
&= -\mathrm{Tr}\ln p\!\!\!/ - \mathrm{Tr}\ln(1 + p\!\!\!/^{-1}M) && \text{(A.4)}\\
&\approx -\mathrm{Tr}\ln p\!\!\!/ - \mathrm{Tr}\left[p\!\!\!/^{-1}M\right] + \frac{1}{2}\mathrm{Tr}\left[p\!\!\!/^{-1}Mp\!\!\!/^{-1}M\right] - \ldots, && \text{(A.5)}
\end{aligned}$$

were we used the shortcut $M = g(\sigma + i\gamma^5\vec{\tau}\vec{\pi})$. Applying $(p\!\!\!/)^{-1} = p\!\!\!//p^2$ and the fact that the trace of an odd number of Dirac matrices vanishes we see that only powers of $p\!\!\!/^{-1}Mp\!\!\!/^{-1}M$ remain in the sum (besides the $\ln p\!\!\!/$-term). Using

$$\begin{aligned}
p\!\!\!/^{-1}Mp\!\!\!/^{-1}M &= \frac{p\!\!\!/}{p^2}g(\sigma + i\gamma^5\vec{\tau}\vec{\pi})\frac{p\!\!\!/}{p^2}g(\sigma + i\gamma^5\vec{\tau}\vec{\pi}) && \text{(A.6)}\\
&= \frac{p\!\!\!/}{p^2}\gamma^\mu g(\sigma - i\gamma^5\vec{\tau}\vec{\pi})\frac{p_\mu}{p^2}g(\sigma + i\gamma^5\vec{\tau}\vec{\pi}) && \text{(A.7)}
\end{aligned}$$

and

$$\phi(x)p_\mu = p_\mu\phi(x) + [\phi(x), p_\mu] = p_\mu\phi(x) - i\partial_\mu\phi(x), \tag{A.8}$$

for any field $\phi(x)$ we arrive at

$$p\!\!\!/^{-1}Mp\!\!\!/^{-1}M = \frac{p\!\!\!/}{p^2}p\!\!\!/g(\sigma - i\gamma^5\vec{\tau}\vec{\pi})\frac{1}{p^2}g(\sigma + i\gamma^5\vec{\tau}\vec{\pi}) - i\frac{p\!\!\!/}{p^2}\left(\partial\!\!\!/ g(\sigma - i\gamma^5\vec{\tau}\vec{\pi})\right)\frac{1}{p^2}g(\sigma + i\gamma^5\vec{\tau}\vec{\pi}). \tag{A.9}$$

Employing the operator identity (for A invertible)

$$[A^{-1}, B] = -A^{-2}[A,B] - A^{-3}[A,[A,B]] - A^{-4}[A,[A,[A,B]]] - \ldots \tag{A.10}$$

with $A = p^2$ and $B = \sigma, \pi$ the $1/p^2$ term in (A.9) can be commuted to the left. The nested commutators in (A.10) are computed by utilizing recursively the identity

$$[p^2, \phi] = \Box\phi + 2ip^\mu\partial_\mu\phi. \tag{A.11}$$

Inspecting (A.11) one sees that each commutator with p^2 contributes at least one derivative of ϕ leading to the observation that terms in (A.10) with n commutators imply at least n derivatives of the meson fields. Thus, we find

$$[p^{-2}, \sigma \text{ or } \pi] = 0 + \mathscr{O}(\partial\sigma, \partial\vec{\pi}) \tag{A.12}$$

leading to

$$\not{p}^{-1}M\not{p}^{-1}M = \frac{1}{p^2}g(\sigma - i\gamma^5\vec{\tau}\vec{\pi})g(\sigma + i\gamma^5\vec{\tau}\vec{\pi}) + \mathscr{O}(\partial\sigma, \partial\vec{\pi}) \tag{A.13}$$

$$= \frac{1}{p^2}m_q^2 + \mathscr{O}(\partial\sigma, \partial\vec{\pi}) \tag{A.14}$$

with $m_q^2 = g^2(\sigma^2 + \vec{\pi}^2)$. Taking only zero derivative terms, the higher powers of $\not{p}^{-1}M\not{p}^{-1}M$ in the expansion (A.5) result in

$$(\not{p}^{-1}M\not{p}^{-1}M)^n = \left(\frac{1}{p^2}\right)^n \left(m_q^2\right)^n \mathbb{1}_D + \mathscr{O}(\partial\sigma, \partial\vec{\pi}) \tag{A.15}$$

with $\mathbb{1}_D$ denoting the unity matrix in Dirac space. Then the complete expansion (A.5) gives

$$\Omega_q = \approx -\mathrm{Tr}\ln\not{p} - \frac{1}{2}\mathrm{Tr}\left[\frac{m_q^2}{p^2}\mathbb{1}_D\right] - \frac{1}{4}\mathrm{Tr}\left[\left(\frac{m_q^2}{p^2}\right)^2 \mathbb{1}_D\right] - \cdots + \mathscr{O}(\partial\sigma, \partial\pi^a). \tag{A.16}$$

It can easily be checked that this is exactly the expansion of a noninteracting Fermi gas with mass m_q

$$-\mathrm{Tr}\ln\left[\not{p} - m_q\right] = -\mathrm{Tr}\ln\not{p} - \sum_n \frac{1}{2n}\mathrm{Tr}\left[\left(\frac{m_q^2}{p^2}\right)^n \mathbb{1}\right], \tag{A.17}$$

thus verifying (13).

Appendix A.2. Inverting perturbed matrices

We apply

$$M^{-1} = M_0^{-1}\sum_{n=0}^{\infty}(-\Delta_M M_0^{-1})^n, \qquad M = M_0 + \Delta_M \tag{A.18}$$

valid for invertible matrices M and M_0. A heuristic derivation of (A.18) can be obtained by noting

$$M^{-1} = (M_0 + \Delta_M)^{-1} = M_0^{-1}(1 - (-M_0\Delta_M))^{-1} \tag{A.19}$$

which is then written as a geometric series, leading to (A.18). With $M_b^a \equiv M(x_a, x_b)$ this relations can be reformulated for the continuum limit in the language of functional derivatives with the only changes being $\partial/\partial\phi_i \to \delta/\delta\phi(x)$ and the matrix multiplication replaced by an integral $A_b^a B_c^b \to \int dbA(x_a, b)B(b, x_c)$.

Appendix A.2.1. Application to the photon propagator

Setting $M(z,z') \equiv \left(\left(G_\gamma^0\right)_{\mu\nu}(z,z')\right)^{-1} = \overline{G}_{\mu\nu}^\gamma(z,z')^{-1} + \left[-e^2\pi^+(z)\pi^-(z)g_{\mu\nu}\right]\delta(z-z')$ one gets

$$\left(G_\gamma^0\right)_{\mu\nu}(z,z') = \overline{G}_{\mu\nu}^\gamma(z,z') + \int d^4x \overline{G}_{\mu\rho}^\gamma(z,x)\left[e^2\pi^+(x)\pi^-(x)g^{\rho\kappa}\right]\overline{G}_{\kappa\nu}^\gamma(x,z') + \mathscr{O}\left(e^4\right), \tag{A.20}$$

which is applied in (31).

Appendix A.2.2. Application to the quark propagator

Setting $M(z,z') \equiv \left(\left(G_\psi^0\right)_{\sigma,\pi}(z,z')\right)^{-1} = \left(G_\psi^0\right)_{\langle\sigma\rangle,0}(z,z')^{-1} + \left[-g\Delta(z) - gi\gamma^5\tau_a\pi^a(z)\right]\delta(z-z')$ one obtains

$$\begin{aligned}\left(G_\psi^0\right)_{\sigma,\pi}(z,z') = &\left(G_\psi^0\right)_{\langle\sigma\rangle,0}(z,z') - \int d^4x \left(G_\psi^0\right)_{\langle\sigma\rangle,0}(z,x)A(x)\left(G_\psi^0\right)_{\langle\sigma\rangle,0}(x,z') \\ &- \iint d^4x d^4y \left(G_\psi^0\right)_{\langle\sigma\rangle,0}(z,x)A(x)\left(G_\psi^0\right)_{\langle\sigma\rangle,0}(x,y)A(y)\left(G_\psi^0\right)_{\langle\sigma\rangle,0}(y,z') \\ &- \iint d^4x d^4y \left(G_\psi^0\right)_{\langle\sigma\rangle,0}(z,y)A(y)\left(G_\psi^0\right)_{\langle\sigma\rangle,0}(y,x)A(x)\left(G_\psi^0\right)_{\langle\sigma\rangle,0}(x,z') + \mathscr{O}\left(\Delta^3, \vec{\pi}^3\right),\end{aligned} \tag{A.21}$$

$$A(z) = -g\Delta(z) - gi\gamma^5\tau_a\pi^a(z). \tag{A.22}$$

Replacing on both sides of the equation $\Delta(z)$ by $\delta/\delta\eta_\sigma(z)$ and $\pi^a(z)$ by $\delta/\delta\eta_{\pi^{-a}}(z)$ one arrives at

$$\begin{aligned}\widehat{G^0_\psi}(z,z') =& \left(G^0_\psi\right)_{\langle\sigma\rangle,0}(z,z') - \int d^4x \left(G^0_\psi\right)_{\langle\sigma\rangle,0}(z,x)\hat{A}(x)\left(G^0_\psi\right)_{\langle\sigma\rangle,0}(x,z') \\ &- \iint d^4x d^4y \left(G^0_\psi\right)_{\langle\sigma\rangle,0}(z,x)\hat{A}(x)\left(G^0_\psi\right)_{\langle\sigma\rangle,0}(x,y)\hat{A}(y)\left(G^0_\psi\right)_{\langle\sigma\rangle,0}(y,z') \qquad (A.23)\\ &- \iint d^4x d^4y \left(G^0_\psi\right)_{\langle\sigma\rangle,0}(z,y)\hat{A}(y)\left(G^0_\psi\right)_{\langle\sigma\rangle,0}(y,x)\hat{A}(x)\left(G^0_\psi\right)_{\langle\sigma\rangle,0}(x,z') + \mathscr{O}\left(\frac{\delta^3}{\delta\eta_\sigma^3},\frac{\delta^3}{\delta\eta_\pi^3}\right),\end{aligned}$$

$$\hat{A}(z) = -g\frac{\delta}{\delta\eta_\sigma(z)} - gi\gamma^5\tau_a\frac{\delta}{\delta\eta_{\pi^{-a}}(z)}, \qquad (A.24)$$

which is used in Section 4.1.

Appendix B. Thermodynamics and phase structure

Appendix B.1. Thermodynamics

Setting all sources to zero in (8) transforms S_η formally into the grand canonical partition function Z. As our goal is to study systems much smaller than the mean free path of photons (which is a reasonable assumption in the context of HICs) the photons do not contribute to the pressure. Thus we remove all terms containing the photon field A from (8), which corresponds to setting zero the electromagnetic coupling e (explicitly and implicitly in J^μ_γ) as well as removing $\det G_\gamma$ from (35). Then we get

$$Z = \sqrt{\det G_\pi}^3 \sqrt{\det G_\sigma}\exp\left\{-\int d^4x\langle U_{\text{eff}}\rangle + \frac{1}{2}m_\pi^2\langle\vec{\pi}^2\rangle + \frac{1}{2}m_\sigma\langle\Delta^2\rangle\right\}. \qquad (B.1)$$

As $\langle U_{\text{eff}}\rangle, \langle\vec{\pi}^2\rangle, \langle\Delta^2\rangle$ and $m_{\sigma,\pi}$ do not depend on the space-time coordinates, the integration in the exponent yields a factor of the Euclidean volume $V\beta$. For the grand canonical potential $\Omega(T,\mu) = -p(T,\mu) = (\beta V)^{-1}\ln Z$ one gets

$$\Omega = \frac{3}{2}\ln\det G_\pi + \frac{1}{2}\ln\det G_\sigma - \langle U_{\text{eff}}\rangle - \frac{1}{2}m_\pi^2\langle\vec{\pi}^2\rangle - \frac{1}{2}m_\sigma\langle\Delta^2\rangle. \qquad (B.2)$$

Applying $\ln\det G_{\pi,\sigma} = \text{Tr}\ln G_{\pi,\sigma}$ and using standard techniques [81] for solving these functional traces one arrives at

$$\Omega = \Omega_\pi + \Omega_\sigma + \langle U\rangle + \langle\Omega_\psi\rangle - \frac{1}{2}m_\pi^2\langle\vec{\pi}^2\rangle - \frac{1}{2}m_\sigma\langle\Delta^2\rangle, \qquad (B.3)$$

$$\Omega_\pi = \frac{3}{3(2\pi)^3}\int dp^3\frac{p^2}{E_\pi}(1+n_B(E_\pi),) \qquad (B.4)$$

$$\Omega_\sigma = \frac{1}{3(2\pi)^3}\int dp^3\frac{p^2}{E_\sigma}(1+n_B(E_\sigma)), \qquad (B.5)$$

$$E^2_{\pi,\sigma} = m^2_{\pi,\sigma} + \vec{p}^2 \qquad (B.6)$$

and Ω_ψ according to (19) in agreement with [64, 78, 79]. From the thermodynamic potential the thermodynamic quantities (energy density, net quark density, entropy density, susceptibilities, etc.) follow by differentiation. The explicit formulas have been worked out in [64, 78, 79].

Appendix B.2. Impact of model parameters on the phase diagram

For the sake of an easy comparison with literature (*cf.* [82] for parameter fixings when including vacuum fluctuations) we choose the parameters as in [64, 72, 78, 79], corresponding to parameter set A in Tab. 1. (The effect of other parameter choices is discussed in [72] for different σ vacuum mass fixings, in [78] for different π vacuum masses and in [83] for the three flavor model w.r.t. explicit symmetry breaking parameters and the σ mass.) The structure of the phase diagram is conform with expectations spelled out in [84]: Isentropic curves as indicators of the paths of fluid elements during adiabatic expansion "go through" the phase border curve. The type IA FOPT (in the nomenclature of [84]) is realized by our model with parameter set A. Such a choice leads to the phase diagram depicted in Fig. B.8 with the CEP coordinates being $T_{\text{CEP}} = 74\,\text{MeV}$ and $\mu_{\text{CEP}} = 278\,\text{MeV}$. Typically (and in fact in all of the above cited references) one or more parameters of the

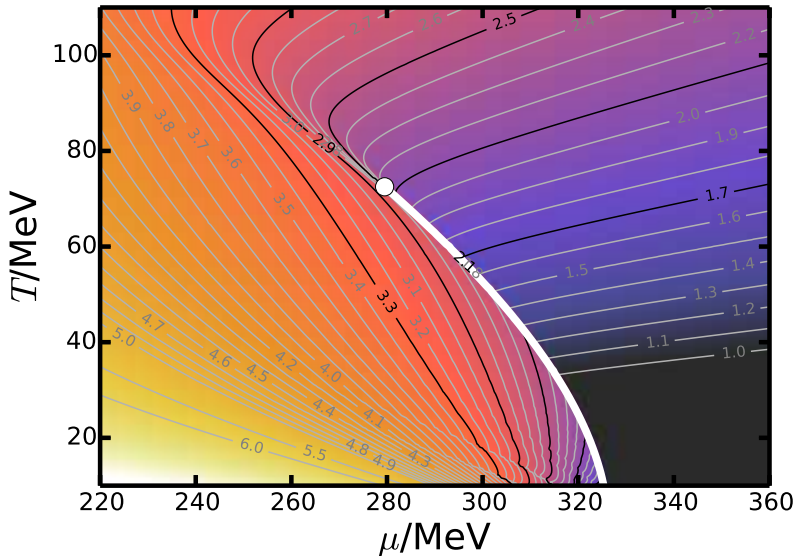

Figure B.8: Contour plot of entropy per quark over the phase diagram for parameter set A in Tab. 1. Also plotted are isentropes (gray and black curves) with their respective s/n values indicated. The black isentropes are those marked in the right panels of Figs. 4-7. The solid white curves depicts the coexistence curve for the FOPT, and the white blob depicts the CEP.

Lagrangian or the vacuum masses are tuned keeping the others fixed to study the impact on various model properties (*e.g.* the CEP). We take a different point of view and work out below which particular combinations of parameters determine certain features of the phase diagram.

Appendix B.3. Phase border curve

The phase transition features (proper FOPT curve and crossover region) are to a large extent determined by the meson potential at zero meson fields. This follows from realizing that the fermionic contribution to the pressure in the chirally restored phase is much larger than the fermionic and bosonic contributions in the chirally broken phase. The difference is compensated at the phase transition curve by a change in the average meson potential switching from $\langle U(\sigma \approx \langle\sigma\rangle_{\rm vac})\rangle$ in the chirally broken phase to $\langle U(\sigma \ll \langle\sigma\rangle_{\rm vac})\rangle$ in the chirally restored phase. Thus

$$-U(\langle\sigma\rangle_{\rm vac}) + \text{Fermi + Bose terms} \approx -U(0) + 2N_f N_c \left(\frac{7}{8}\frac{\pi^2}{90}T^4 + \frac{1}{24}\mu^2 T^2 + \frac{1}{48\pi^2}\mu^4\right), \tag{B.7}$$

$$\begin{aligned} U(0) &= \frac{\langle\sigma\rangle_{\rm vac}{}^2}{8}\frac{\left((m_\sigma^{\rm vac})^2 - 3(m_\pi^{\rm vac})^2\right)^2}{(m_\sigma^{\rm vac})^2 - (m_\pi^{\rm vac})^2} \\ &= \frac{(m_\sigma^{\rm vac})^2\langle\sigma\rangle_{\rm vac}{}^2}{8}\left(1 - 5\frac{m_\pi^{\rm vac2}}{m_\sigma^{\rm vac2}} + \mathscr{O}\left(\frac{m_\pi^{\rm vac4}}{m_\sigma^{\rm vac4}}\right)\right), \end{aligned} \tag{B.8}$$

$$U(\langle\sigma\rangle_{\rm vac}) = \frac{(m_\sigma^{\rm vac})^2\langle\sigma\rangle_{\rm vac}{}^2}{8}\left(-8\frac{(m_\pi^{\rm vac})^2}{(m_\sigma^{\rm vac})^2} + \mathscr{O}\left(\frac{m_\pi^{\rm vac4}}{m_\sigma^{\rm vac4}}\right)\right) \tag{B.9}$$

give as an estimate for the critical temperature w.r.t. the chemical potential $T_c(\mu)$

$$T_c^2 = \frac{1}{7\pi^2}\left(2\sqrt{30}\sqrt{\frac{42\pi^2(U(0) - U(\langle\sigma\rangle_{\rm vac}))}{2N_f N_c} + \mu^4} - 15\mu^2\right). \tag{B.10}$$

Since we keep $(m_\pi^{\rm vac})^2/(m_\sigma^{\rm vac})^2$ small in order to maintain realistic scenarios one may apply the chiral limit value of $U(0) - U(\langle\sigma\rangle_{\rm vac}) = (m_\sigma^{\rm vac})^2\langle\sigma\rangle_{\rm vac}{}^2/8$ as a good estimate. Although this estimate looks quite crude and in the crossover region not even justified it is a surprisingly accurate result for the phase transition curve (*cf.* Fig. B.9). Inspecting Fig. B.9 one notes that although the model parameters, *e.g.* $\langle\sigma\rangle_{\rm vac}$, individually vary by a factor of two the form and position of the phase contour changes only slightly as long as $m_\sigma^{\rm vac}\langle\sigma\rangle_{\rm vac}$ is kept fixed. Changing $m_{\rm nuc}^{\rm vac}$ has only small effect, too, at least if the difference between the critical chemical

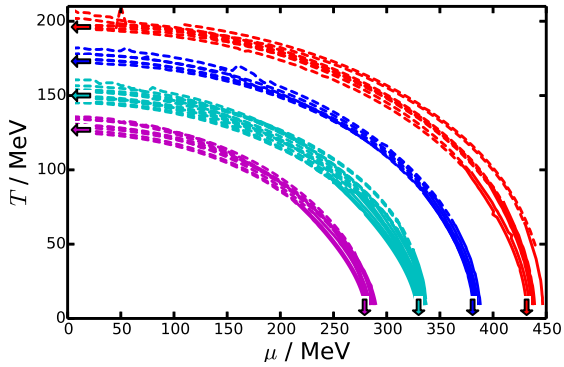

Figure B.9: Critical curves (FOPT: solid, crossover estimate: dashed) for several parameter sets varying $\langle\sigma\rangle_{\rm vac}$ in the range of 60 MeV to 120 MeV and $\mu_c^0 - m_{\rm nuc}^{\rm vac}/3$ from -100 MeV to 100 MeV. In each group of (phase) transition curves, $m_\sigma^{\rm vac}\langle\sigma\rangle_{\rm vac}$ is kept fixed at $m_\sigma^{\rm vac}\langle\sigma\rangle_{\rm vac}/\,{\rm GeV}^2 = 0.1156$ (red), 0.09 (dark blue), 0.0676 (light blue) and 0.048 (violet). The arrows denoting the pseudocritical temperature at vanishing density, $T_{\rm pc}^0$, and the critical chemical potential at vanishing temperature, μ_c^0, are calculated according to (B.12) for the respective (same color) group of phase contours with fixed $m_\sigma^{\rm vac}\langle\sigma\rangle_{\rm vac}$.

potential μ_c^0 at $T = 0$ and the vacuum quark mass $m_{\rm nuc}^{\rm vac}/3$ is sufficiently small. (In Fig. B.9 its absolute value is kept smaller than 100 MeV.) Analyzing further parameter sets we find that for $\mu_c^0 - m_{\rm nuc}^{\rm vac}/3 \gtrsim 100$ MeV the CEP disappears, *cf.* left panel of Fig. B.11 for the dependence of the CEP temperature on this particular parameter combination. We are able to trace the disappearance of the CEP back to the Fermi pressure, which - for $\mu_c^0 - m_{\rm nuc}^{\rm vac}/3$ being large enough - can compensate the difference of the meson potentials in both phases and thus reduces the strength of the FOPT. For $\mu_c^0 - m_{\rm nuc}^{\rm vac}/3 < -100$ MeV there is the tendency to reduce the curvature of the phase contour, because for a higher quark mass scale, the Fermi pressure gets less important and the pressure in the chirally broken phase is more influenced by the pressure of the pions, which changes the μ-dependence of the phase border curve. To achieve more quantitative agreement for the pseudocritical temperature at vanishing density, T_c^0, and the critical chemical potential at zero temperature, μ_c^0, it is convenient to scale the prediction according to (B.10) with $m_\pi^{\rm vac} = 0$ with the result for some reference parameter set. In Fig. B.9 we chose

$$T_{\rm pc}^{0,\rm ref} = 150\,{\rm MeV}, \qquad \mu_c^{0,\rm ref} = 330\,{\rm MeV} \qquad \text{for } m_\sigma^{\rm vac}\langle\sigma\rangle_{\rm vac} = 260^2\,{\rm MeV}^2. \tag{B.11}$$

Inspecting (B.10) yields $T_c^0, \mu_c^0 \propto \sqrt{m_\sigma^{\rm vac}\langle\sigma\rangle_{\rm vac}}$, thus such a scaling gives the estimates

$$T_{\rm pc}^0 \approx 150\,{\rm MeV}\frac{\sqrt{m_\sigma^{\rm vac}\langle\sigma\rangle_{\rm vac}}}{260\,{\rm MeV}}, \qquad \mu_c^0 \approx 330\,{\rm MeV}\frac{\sqrt{m_\sigma^{\rm vac}\langle\sigma\rangle_{\rm vac}}}{260\,{\rm MeV}}. \tag{B.12}$$

In Fig. B.9 these estimates are depicted as small arrows and show good agreement with the actual positions of the FOPT and the crossover curve.

Appendix B.4. Isentropes

The pattern of isentropes depends, as the CEP and the FOPT details, on the model parameters. Figure B.8 (for set A) exhibits an example where the CEP acts as an attractor for some isentropes. Such a pattern, sometimes called "focusing effect" is discussed in [21, 85, 86] with the outcome of not being a necessarily accompanying feature of a CEP. We emphasize that isentropes provide an interesting supplementing analytical information beyond the plain FOPT curve and the CEP position in the phase diagram. On the FOPT curve isentropes with different s/n ratios can run partially on top of each other. This reflects the fact that the state the model resides in is not uniquely defined on a FOPT but may differ in the phase decomposition. Physical properties of the medium on the FOPT curve are therefore determined as the average (based on *e.g.* the volume fraction) of the respective quantity over the coexisting phases. Such a procedure is applied also in Figs. 4-7 for the photon rates.

The behavior of the isentropes can be calculated analytically in the limits of $T \to 0$ as well as $m_q \to 0$. In the high temperature phase, the pressure of the model is well approximated by the pressure of an ideal massless Fermi gas minus the meson potential at zero fields $U(\sigma = 0, \pi = 0)$. For this, the entropy per baryon can be

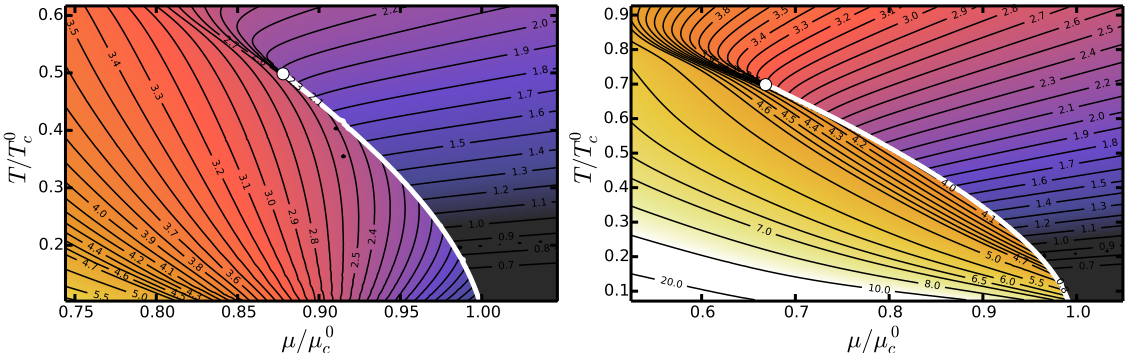

Figure B.10: Phase diagrams for parameter choices according to parameter sets B (left panel) and C (right panel), *cf.* Tab. 1. T is scaled by the pseudocritical temperature T_c^0 at $\mu = 0$ and μ by the critical chemical potential μ_c^0 at $T = 0$. (T_c^0 and μ_c^0 are given in Tab. 1). For the left panel $m_{\rm nuc}^{\rm vac}/3\mu_c^0 = 0.907$ and for the right panel $m_{\rm nuc}^{\rm vac}/3\mu_c^0 = 1.111$. The black curves are the isentropes labeled by their corresponding ratio s/n. Shifting $m_q^{\rm vac}$ relative to $m_\sigma^{\rm vac} f_\pi$ changes the dynamics of the model qualitatively. Definition of the FOPT curve (solid white curve) and CEP (white dot) as for Fig. 4.

easily calculated leading to

$$\frac{s}{n} = \pi^2 \frac{7\pi^2 \tan^3(\phi) + 15\tan(\phi)}{15\pi^2 \tan^2(\phi) + 15}, \tag{B.13}$$

with $\tan(\phi) = T/\mu$. The meson contributions are suppressed because they acquire large masses in the hot and dense phase [15]. According to (B.13) for every choice of s/n the isentropes of an ideal massless Fermi gas, and thus for the QMM in the high temperature phase, follow curves with $\tan(\phi)$=const, *i.e.* straight lines pointing to $\mu = T = 0$.

The isentropes at $T \to 0$ can be obtained by considering the various contributions in (B.3) to the thermodynamic potential. It turns out that the only non-vanishing term at $T = 0$ in (B.3) is the (averaged) fermion pressure at $\mu \geq m_q^{\rm vac} \equiv m_{\rm nuc}^{\rm vac}/3$. Approximating the Fermi distribution function for small T and $(\mu - m_q^{\rm vac})$ one can show that all isentropes approach the point $(T = 0, \mu_1 = m_q^{\rm vac})$ in the phase diagram, at least if vacuum fluctuations are not included (as in this work). In Appendix B.3 we discuss the dependency of the phase transition curve w.r.t. the model parameters finding that to a large extent, the critical chemical potential at $T = 0$ is determined by the the combination $m_\sigma^{\rm vac}\langle\sigma\rangle_{\rm vac}$. Thus by tuning the model parameters (or equivalently the vacuum values for the pion and quark masses as well as $\langle\sigma\rangle_{\rm vac}$, *cf.* (51)) the endpoints of the isentropes and the FOPT curve can be shifted relative to each other making the model flexible enough for the study of different dynamical situations, *i.e.* the adiabatic expansion paths are either "going trough", or "sticking to" the FOPT curve, corresponding to types IA and II in the nomenclature of [84]. It turns out that within this model it is not possible by parameter tuning to shift these endpoints into the high-density phase. In Fig. B.10 this behavior is visualized. In the left panel the isentropes approach the point $T/T_c^0, \mu/\mu_c^0 = (0, 0.907)$ which is precisely the point $(0, m_q^{\rm vac})$ as claimed for the case that $m_q^{\rm vac} < \mu_c^0$. In the right panel $m_q^{\rm vac} > \mu_c^0$ and thus the isentropes all merge with the FOPT at low enough temperatures.

Appendix B.5. Critical end point

To get a feeling for what determines the position of the CEP within this model one may resort to the mean field approximation[1]. In this approximation the meson dependence of the pressure is only via the expectation

[1]There is a large difference between the CEP position when comparing approximations with and without vacuum fluctuations [86]. However, when comparing approximations with and without mesonic fluctuations the shift is much smaller and the qualitative dependence on the model parameters is similar.

value v of the sigma field:

$$p_{\rm MFA}(v) = -\frac{\lambda}{4}(v^2-\zeta)^2 + Hv - \frac{2N_fN_cT}{(2\pi)^3}\int d^3p\left[\ln\left(1+e^{(\mu-E)/T}\right)+\{\mu\to-\mu\}\right], \tag{B.14}$$

$$\begin{aligned} 0 &= \frac{\partial p_{\rm MFA}}{\partial v} \\ &= -\lambda(v^2-\zeta)v + H + \frac{2N_fN_cg^2v}{2\pi^2}\int dp\frac{p^2}{E}(n_F(E)+n_{\overline{F}}(E)) \end{aligned} \tag{B.15}$$

with $n_{F,\overline{F}} = (1+\exp\{(E\mp\mu)/T\})^{-1}$ denoting the distribution functions for fermions (-) and antifermions (+). The occurrence of a FOPT and the position of the CEP are understandable in view of (B.15). A FOPT requires (at least) triple solutions of (B.15). One of this solutions has a small v leading to a dominant fermion term and corresponding to the chirally restored phase. One solution is thermodynamically unstable, and the third is relatively close to the vacuum value corresponding to the chirally broken phase. For this solution, the derivative of the meson potential gives important contributions.

At zero temperature, two cases can be distinguished: (i) The fermion mass $m_q = gv$ close to the critical curve (or its estimate according to (B.10)) is so small that the fermionic integral in (B.15) is dominant already. Then no FOPT occurs. In the opposite case, the mass can still be smaller than the critical chemical potential (case (iia)) or greater (or equal) to it (case (iib)). In both cases there is a FOPT. According to (B.10) the critical curve bends toward the temperature axis and already at relatively small T the critical chemical potential is smaller than the vacuum fermion mass. Thus we discuss only case (iib) and regard it as an upper limit for (iia). For (iib), substantial contributions to the fermion integral origin from the edge of the Fermi distributions or their proximity, *i.e.* the range $(\mu - xT, \mu + xT)$ and $x = 2\ldots4$. Since the minimal argument for the Fermi distributions is m_q the contributing interval is $[m_q, \mu + xT)$. If the vacuum quark mass is larger than $\mu + xT$ the fermion integral is too small to be of significance. Inserting $\mu_c(T)$ according to (B.10) and $x = 4$ evidences for $m_{\rm nuc}^{\rm vac} \gtrsim 1680\,{\rm MeV}$ (for the parameter set $m_\sigma^{\rm vac} = 700\,{\rm MeV}$, $m_\pi^{\rm vac} = 138\,{\rm MeV}$, $\langle\sigma\rangle_{\rm vac} = 92.4\,{\rm MeV}$) that the fermion integral is small for all temperatures at the critical curve yielding a FOPT surrounding the chirally broken phase completely. This provides an important observation: If the quark mass is sufficiently large compared to the critical chemical potential $\mu_c(T)$ whose values are in turn determined by the parameter combination $m_\sigma^{\rm vac}\langle\sigma\rangle_{\rm vac}$, the FOPT curve can be made to extend from the μ axis even to the T axis. On the other hand, a large fermion mass means that the isentropes end on the critical curve (see discussion above), which is typically not a desired feature and, if one needs isentropes to exit the critical curve at some non-zero temperature, one cannot use a parameter set with arbitrary large fermion mass, but is limited to a mass less than the critical chemical potential at zero temperature (determined from (B.10)). Then, there is an upper limit for the critical temperature corresponding to a CEP at $T_{\rm CEP} = \mathcal{O}(100\,{\rm MeV})$ and corresponding $\mu_{\rm CEP}$.

With these considerations the behavior of the temperature $T_{\rm CEP}$ of the CEP (*i.e.* increasing the vacuum fermion mass $m_{\rm nuc}^{\rm vac}/3$ increases $T_{\rm CEP}$, *cf.* left panel of Fig. B.11) is understandable. The chemical potentials of the various critical points collapse to one line if one assumes that the quark mass at the phase contour is about 1/2 of its vacuum value (which works reasonable well, *cf.* right panel of Fig. B.11). As discussed in [79] the QMM with linearized fluctuations exhibits a fuzzy structure at the CEP. It is therefore more appropriate to speak of a "CEP-region" which is hidden under the white blobs in Figs. 4-B.8 and B.10. Hence, we focus on the FOPT and leave the CEP related issues untouched.

Appendix C. Matrix elements

We quote here the matrix elements implemented in the calculations presented in Section 5. They have been checked with the CompHEP package [87] and fulfill the corresponding Ward identities. With the incoming momenta labeled by p_q (quarks), p_m (mesons) and the outgoing momenta q_q (quarks) and k (photon) and the Mandelstam variables defined as $s = (p_q + p_m)^2$, $t = (p_q - q_q)^2$ and $u = (p_q - k)^2$ the fully (spin, polarization, flavor) summed and averaged matrix elements for the Compton processes are given below.

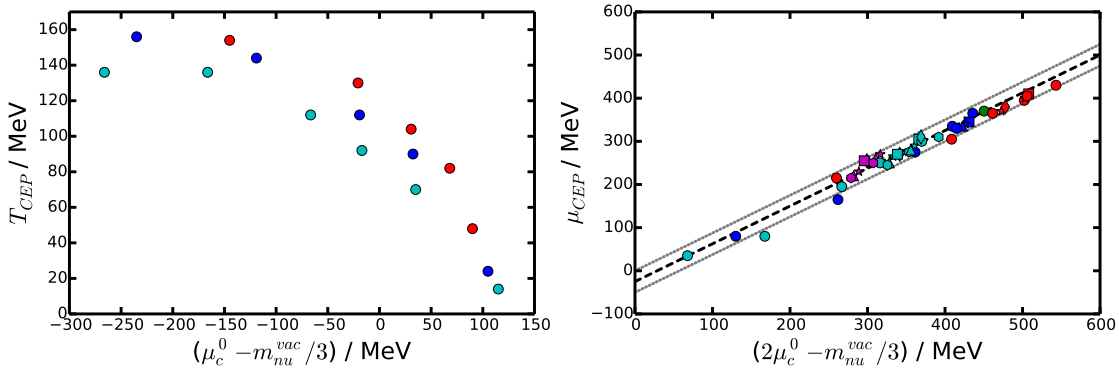

Figure B.11: Dependence of the CEP coordinates ($T_{\rm CEP}$ in the left panel and $\mu_{\rm CEP}$ in the right) on model parameters. The color code is the same as in Fig. B.9. The symbols denote $\langle\sigma\rangle_{\rm vac}/\,{\rm MeV} = 60$ (hexagons), 70 (triangles), 90 (stars), 100 (circles), 110 (squares), 120 (diamonds). The black dashed line depicts the function $f(x) = -50\,{\rm MeV} + 7x/8$ with $x = 2\mu_c^0 - m_{\rm nuc}^{\rm vac}/3$ and the gray dotted lines are for $f_\pm = f(x) \pm 25\,{\rm MeV}$.

Appendix C.1. Compton scattering $q+\pi \to q+\gamma$

$$\frac{1}{2}\sum|\mathscr{M}_{q\pi\to q\gamma}|^2 = e^2g^2\left(-\frac{10}{3}\left(\frac{s-m_q^2}{u-m_q^2}+\frac{u-m_q^2}{s-m_q^2}\right)+\frac{20}{3}m_\pi^2m_q^2\left(\frac{1}{(u-m_q^2)^2}+\frac{1}{(s-m_q^2)^2}\right)\right.$$
$$\left.+\frac{4}{3}-\frac{4}{3}\frac{m_\pi^2(s+u-m_\pi^2)}{(u-m_q^2)(s-m_q^2)}+8\frac{m_\pi^2 t}{t-m_\pi^2}\left(\frac{1}{u-m_q^2}+\frac{1}{s-m_q^2}+\frac{2}{t-m_\pi^2}\right)\right), \qquad \text{(C.1)}$$

with $\sum|\mathscr{M}_{q\pi\to q\gamma}|$ denoting the spin, flavor and polarization summed matrix elements. The factor $1/2$ is due to averaging over incoming flavors. For the case of massless pions (*i.e.* in the broken phase in the chiral limit) one finds

$$\frac{1}{2}\sum|\mathscr{M}_{q\pi\to q\gamma}|^2 = e^2g^2\left(-\frac{10}{3}\left(\frac{s-m_q^2}{u-m_q^2}+\frac{u-m_q^2}{s-m_q^2}\right)+\frac{4}{3}\right). \qquad \text{(C.2)}$$

Appendix C.2. Compton scattering $q+\sigma \to q+\gamma$

$$\frac{1}{2}\sum|\mathscr{M}_{q\sigma\to q\gamma}|^2 = -\frac{5}{9}g^2e^2\left((4m^2-m_\sigma^2)\left(\frac{4m^2}{(u-m_q^2)^2}+\frac{4m^2}{(s-m_q^2)^2}+\frac{4(2m^2-m_\sigma^2)}{(u-m_q^2)(s-m_q^2)}\right)\right.$$
$$\left.+2\frac{s+7m^2-2m_\sigma^2}{u-m_q^2}+2\frac{u+7m^2-2m_\sigma^2}{s-m_q^2}+4\right). \qquad \text{(C.3)}$$

If the fermion masses are set to zero (corresponding to the restored phase in the chiral limit), this reduces to:

$$\frac{1}{2}\sum|\mathscr{M}_{q\sigma\to q\gamma}|^2 = -\frac{5}{9}g^2e^2\left(4\frac{m_\sigma^4}{us}+2\frac{s-2m_\sigma^2}{u}+2\frac{u-2m_\sigma^2}{s}+4\right). \qquad \text{(C.4)}$$

Appendix C.3. Annihilation $q+\sigma,\pi \to q+\gamma$

The annihilation matrix elements are related to the Compton matrix elements (C.1) and (C.3) by crossing symmetries and can be obtained by $s \leftrightarrow t$. The matrix elements for the anti-Compton processes (45) are identical to those for the Compton processes (44).

References

[1] H.-T. Ding, F. Karsch, and S. Mukherjee, Int. J. Mod. Phys. **E24**, 1530007 (2015).

[2] C. Pinke and O. Philipsen, PoS **LATTICE2015**, 149 (2016).

[3] Y. Aoki, Z. Fodor, S. D. Katz, and K. K. Szabo, Phys. Lett. **B643**, 46 (2006).

[4] A. Bazavov et al., Phys. Rev. **D85**, 054503 (2012).

[5] Z. Fodor and S. D. Katz, Phys. Lett. **B534**, 87 (2002).

[6] P. de Forcrand and O. Philipsen, Nucl. Phys. **B642**, 290 (2002).

[7] Z. Fodor, S. D. Katz, and C. Schmidt, JHEP **03**, 121 (2007).

[8] O. Kaczmarek et al., Phys. Rev. **D83**, 014504 (2011).

[9] M. A. Stephanov, Prog. Theor. Phys. Suppl. **153**, 139 (2004).

[10] T. Anticic et al., Phys. Rev. **C81**, 064907 (2010).

[11] B. Mohanty, Nucl. Phys. **A830**, 899C (2009).

[12] R. A. Lacey, Phys. Rev. Lett. **114**, 142301 (2015).

[13] T. Czopowicz, PoS **CPOD2014**, 054 (2015).

[14] C. S. Fischer, J. Luecker, and C. A. Welzbacher, Phys. Rev. **D90**, 034022 (2014).

[15] O. Scavenius, A. Mocsy, I. N. Mishustin, and D. H. Rischke, Phys. Rev. **C64**, 045202 (2001).

[16] B.-J. Schaefer and J. Wambach, Nucl. Phys. **A757**, 479 (2005).

[17] B.-J. Schaefer, J. M. Pawlowski, and J. Wambach, Phys. Rev. **D76**, 074023 (2007).

[18] T. K. Herbst, J. M. Pawlowski, and B.-J. Schaefer, Phys. Lett. **B696**, 58 (2011).

[19] K. Fukushima and C. Sasaki, Prog. Part. Nucl. Phys. **72**, 99 (2013).

[20] P. Kovács, Z. Szép, and G. Wolf, Phys. Rev. **D93**, 114014 (2016).

[21] M. Bluhm and B. Kämpfer, PoS **CPOD2006**, 004 (2006).

[22] M. A. Stephanov, K. Rajagopal, and E. V. Shuryak, Phys. Rev. **D60**, 114028 (1999).

[23] M. Asakawa, U. W. Heinz, and B. Müller, Phys. Rev. Lett. **85**, 2072 (2000).

[24] V. Vovchenko, D. V. Anchishkin, M. I. Gorenstein, and R. V. Poberezhnyuk, Phys. Rev. **C92**, 054901 (2015).

[25] S. Gupta, PoS **CPOD2009**, 025 (2009).

[26] T. Klahn et al., Phys. Rev. **C74**, 035802 (2006).

[27] D. Teaney, J. Lauret, and E. V. Shuryak, Phys. Rev. Lett. **86**, 4783 (2001).

[28] E. L. Bratkovskaya et al., Phys. Rev. **C69**, 054907 (2004).

[29] Yu. B. Ivanov, V. N. Russkikh, and V. D. Toneev, Phys. Rev. **C73**, 044904 (2006).

[30] P. Romatschke and U. Romatschke, Phys. Rev. Lett. **99**, 172301 (2007).

[31] C. Gale, Landolt-Börnstein **23**, 445 (2010).

[32] R. Rapp, J. Wambach, and H. van Hees, Landolt-Börnstein **23**, 134 (2010).

[33] G. Vujanovic et al., Phys. Rev. **C89**, 034904 (2014).

[34] C. Shen, U. W. Heinz, J.-F. Paquet, and C. Gale, Phys. Rev. **C89**, 044910 (2014).

[35] C.-H. Lee and I. Zahed, Phys. Rev. **C90**, 025204 (2014).

[36] S. A. Bass et al., Prog. Part. Nucl. Phys. **41**, 255 (1998).

[37] W. Cassing and E. L. Bratkovskaya, Nucl. Phys. **A831**, 215 (2009).

[38] B. Bäuchle and M. Bleicher, Phys. Rev. **C82**, 064901 (2010).

[39] O. Linnyk, W. Cassing, and E. L. Bratkovskaya, Phys. Rev. **C89**, 034908 (2014).

[40] W. Liu and R. Rapp, Nucl. Phys. **A796**, 101 (2007).

[41] H. van Hees, C. Gale, and R. Rapp, Phys. Rev. **C84**, 054906 (2011).

[42] S. Turbide, R. Rapp, and C. Gale, Phys. Rev. **C69**, 014903 (2004).

[43] I. Tserruya, Landolt-Börnstein **23**, 176 (2010).

[44] R. Rapp, H. van Hees, and M. He, Nucl. Phys. **A931**, 696 (2014).

[45] C. Gale et al., Phys. Rev. Lett. **114**, 072301 (2015).

[46] H. van Hees, M. He, and R. Rapp, Nucl. Phys. **A933**, 256 (2015).

[47] V. Vovchenko et al., Phys. Rev. **C94**, 024906 (2016).

[48] A. Lesne, *Renormalization Methods: Critical Phenomena, Chaos, Fractal Structures*, Wiley, Berlin, 2011.

[49] N. G. Antoniou, F. K. Diakonos, A. S. Kapoyannis, and K. S. Kousouris, Phys. Rev. Lett. **97**, 032002 (2006).

[50] J. Delorme, M. Ericson, A. Figureau, and N. Giraud, Phys. Lett. **B89**, 327 (1980).

[51] J. Steinheimer, J. Randrup, and V. Koch, Phys. Rev. **C89**, 034901 (2014).

[52] D. Parganlija, F. Giacosa, and D. H. Rischke, Phys. Rev. **D82**, 054024 (2010).

[53] D. Parganlija, P. Kovacs, G. Wolf, F. Giacosa, and D. H. Rischke, Phys. Rev. **D87**, 014011 (2013).

[54] W. I. Eshraim, F. Giacosa, and D. H. Rischke, Eur. Phys. J. **A51**, 112 (2015).

[55] C. Sasaki, Phys. Rev. **D90**, 114007 (2014).

[56] R. Stiele and J. Schaffner-Bielich, Phys. Rev. **D93**, 094014 (2016).

[57] C. Sasaki and I. Mishustin, Phys. Rev. **C85**, 025202 (2012).

[58] V. K. Tiwari, Phys. Rev. **D86**, 094032 (2012).

[59] G. N. Ferrari, A. F. Garcia, and M. B. Pinto, Phys. Rev. **D86**, 096005 (2012).

[60] A. J. Mizher, M. Chernodub, and E. S. Fraga, Phys. Rev. **D82**, 105016 (2010).

[61] K. Kamikado and T. Kanazawa, JHEP **01**, 129 (2015).

[62] K. Paech, H. Stoecker, and A. Dumitru, Phys. Rev. **C68**, 044907 (2003).

[63] C. Herold, M. Nahrgang, I. Mishustin, and M. Bleicher, Phys. Rev. **C87**, 014907 (2013).

[64] A. Mocsy, I. Mishustin, and P. Ellis, Phys. Rev. **C70**, 015204 (2004).

[65] M. Peskin and D. Schroeder, *An Introduction To Quantum Field Theory*, Westview Press, 1995.

[66] J. Zinn-Justin, *Quantum Field Theory and Critical Phenomena*, Clarendon Press, Oxford, 1993.

[67] L. D. Faddeev and V. N. Popov, Phys. Lett. **B25**, 29 (1967).

[68] C. M. Fraser, Z. Phys. **C28**, 101 (1985).

[69] I. J. R. Aitchison and C. M. Fraser, Phys. Rev. **D31**, 2605 (1985).

[70] H. A. Weldon, Phys. Rev. **D28**, 2007 (1983).

[71] L. D. McLerran and T. Toimela, Phys. Rev. **D31**, 545 (1985).

[72] F. Wunderlich and B. Kämpfer, PoS **CPOD2014**, 027 (2015).

[73] K. A. Olive et al., Chin. Phys. **C38**, 090001 (2014).

[74] M. Heffernan, P. Hohler, and R. Rapp, Phys. Rev. **C91**, 027902 (2015).

[75] P. B. Arnold, G. D. Moore, and L. G. Yaffe, JHEP **12**, 009 (2001).

[76] O. Linnyk, V. Konchakovski, T. Steinert, W. Cassing, and E. L. Bratkovskaya, Phys. Rev. **C92**, 054914 (2015).

[77] R.-A. Tripolt, N. Strodthoff, L. von Smekal, and J. Wambach, Phys. Rev. **D89**, 034010 (2014).

[78] E. S. Bowman and J. I. Kapusta, Phys. Rev. **C79**, 015202 (2009).

[79] L. Ferroni, V. Koch, and M. B. Pinto, Phys. Rev. **C82**, 055205 (2010).

[80] F. Wunderlich and B. Kämpfer, J. Phys. Conf. Ser. **599**, 012019 (2015).

[81] J. I. Kapusta and C. Gale, *Finite-temperature field theory: Principles and applications*, Cambridge University Press, 2011.

[82] S. Carignano, M. Buballa, and W. Elkamhawy, Phys. Rev. **D94**, 034023 (2016).

[83] B.-J. Schaefer and M. Wagner, Phys. Rev. **D79**, 014018 (2009).

[84] F. Wunderlich, R. Yaresko, and B. Kämpfer, J. Mod. Phys. **7**, 852 (2016).

[85] C. Nonaka and M. Asakawa, Phys. Rev. **C71**, 044904 (2005).

[86] E. Nakano, B. J. Schaefer, B. Stokic, B. Friman, and K. Redlich, Phys. Lett. **B682**, 401 (2010).

[87] A. Pukhov et al., arXiv:9908288 [hep-ph] (1999).